
Study of the stability of a large realistic cyclonic eddy

de Marez Charly ^{1,*}, Meunier Thomas ², Morvan Mathieu ¹, L'hégaret Pierre ¹, Carton Xavier ¹

¹ Univ. Brest, Laboratoire d'Océanographie Physique et Spatiale (LOPS), IUEM, Rue Dumont D'urville, 29280 Plouzané, France

² CICESE, Ensenada, B.C., Mexico

* Corresponding author : Charly de Marez, email address : charly.demarez@univ-brest.fr

Abstract :

We investigate the stability of a composite cyclone representative of Arabian Sea eddies using a high resolution primitive equation model. We observe that the eddy is unstable with respect to a mixed barotropic/baroclinic instability, leading to the growth of an azimuthal mode 2 perturbation. The latter deforms the eddy, which eventually evolves into a tripole after about 4 months of simulation. The presence of a critical level for the most unstable mode generates sharp fronts in the surface mixed layer where the Rossby number is large. These fronts then become unstable, and this generates submesoscale cyclones and filaments. Near these fronts, diapycnal mixing occurs, causing the potential vorticity to change sign locally, and symmetric instability to develop in the core of the cyclonic eddy. Despite the instabilities, the eddy is not destroyed and remains a large-scale coherent structure for the last 6 months of the simulation. Looking at Sea Surface Height only, the composite eddy evolves little, and fairly represents the eddy observed in the altimetry which can live for several months. The study of this simulation thus illustrates the numerous kinds of instabilities which may occur in large cyclonic eddies but can not be captured directly by altimetric data.

Highlights

► A composite cyclone representative of the Arabian Sea eddies is unstable with respect to a mixed barotropic/baroclinic instability. ► Submesoscale features are generated at the surface via barotropic, baroclinic, and symmetric instabilities. ► Currently available altimetric and floats data cannot capture the instability occurring in the eddy.

Keywords : Mesoscale, Eddy, Instability, Submesoscale, Vortex

1. Introduction

Mesoscale eddies are a prominent feature of the ocean circulation. They have a strong influence on biological activity (Chelton et al., 2011), tracer transport (Zhang et al., 2014), and physical and chemical properties of the water column (Dong et al., 2014). Examples of long lived, coherent, and recurrent mesoscale eddies can be found in every oceanic basin: Gulf Stream rings in the western North Atlantic (Richardson, 1983), meddies in the eastern North Atlantic (Armi et al., 1989), Agulhas rings in the South Atlantic (Olson & Evans, 1986), Mozambique channel eddies in the Indian Ocean (Halo et al., 2014), Kuroshio rings in the western North Pacific (Li et al., 1998), Loop Current Eddies in the Gulf of Mexico (Meunier et al., 2018), the Ras al Hadd dipole in the northern Arabian Sea (L'Hégaret et al., 2015, 2016). All play an important role in the transport of heat and salt.

Mesoscale eddies have been intensively studied over the past 60 years. In particular, many studies have focused on their stability properties, using linear stability analysis (Gent & McWilliams, 1986; McWilliams et al., 1986; Nguyen et al., 2012; Yim & Billant, 2015), and numerical models to study the finite amplitude evolution of unstable perturbations (Carton & McWilliams, 1989; Stegner & Dritschel, 2000; Ménesguen et al., 2018). In these studies, eddies are modelled using analytical profiles, *e.g.* shielded vortices, Rankine vortices (Carton & McWilliams, 1989; Stegner & Dritschel, 2000), Gaussian vortices (McWilliams, 1985), or Lorentzian vortices (Hua et al., 2013; Meunier et al., 2018) assuming that they represent a large range of observed eddies (Le Vu et al., 2018). The result of these stability analyses is strongly dependent on the initial profile imposed. In most cases, the eddy profiles are unstable, and can lead to the destruction of the eddy, the formation of dipoles, tripoles, or the long-time decay of the eddy (Carton et al., 1989; Stegner & Dritschel, 2000).

The increase of computational capabilities has led recent studies to implement very high resolution stability analyses in a 3D context. This allows the study of vortex stability beyond balanced mesoscale processes, and to observe how submesoscale features can emerge from the destabilization of mesoscale structures (Brannigan et al., 2017; Ménesguen et al., 2018). Such studies highlight a possible mechanism for the forward cascade of energy toward small scales.

In the past few years, it has become possible to determine the actual shape of oceanic

31 eddies with a fairly good spatio-temporal resolution. Gridded multi-satellite altimetric prod-
32 ucts provide increased horizontal resolution (up to $1/8^\circ$) and resolve more accurately eddies
33 with radii two or three times the first baroclinic Rossby radius of deformation (R_D hereafter)
34 than older products with coarser horizontal resolution ($1/3^\circ$ or $1/4^\circ$). The rapid growth of
35 the Argo database as well as the increase of the resolution of the vertical profiles signifi-
36 cantly improved the sampling of the vertical structure of the global ocean. Combining the
37 Argo and altimetry datasets, Chaigneau et al. (2011) have shown that *composite* methods
38 are efficient in determining the average 3D shape of eddies and isolating classes of eddies in
39 given areas. This effort has been made in several regions, *e.g.* Chaigneau et al. (2011) in the
40 eastern South Pacific Ocean, Keppler et al. (2018) in the Southwest Tropical Pacific ocean,
41 and de Marez et al. (2019) in the Arabian Sea. In the latter study, the authors computed
42 a composite eddy without *a priori* assumptions (*e.g.* a Gaussian pressure/velocity profile)
43 and only from *in situ* measurements. Because the composite is a mean of a very varied
44 population, it may not in fact be representative of all individual element of the population.
45 However, through comparison with altimetric and *in situ* —drifters, floats, and ship— mea-
46 surements, authors showed that the composite cyclonic eddy is fairly representative of the
47 Arabian Sea’s mesoscale cyclones already observed.

48 In this paper, we investigate the stability of a composite eddy, by running a high resolu-
49 tion primitive equation model initialized with a composite cyclone computed in the Arabian
50 Sea. Contrary to previous studies, we do not use analytical initial conditions. The Arabian
51 Sea, in the northern Indian Ocean, between the African and Asian landmasses, is a region
52 dominated by the monsoon wind regime. This regime leads to seasonal along-shore current
53 reversals. The alongshore currents destabilize and form meanders with 100-200 km wave-
54 lengths which eventually detach to form eddies with similar diameters (Schott & McCreary,
55 2001). Wind forcing and baroclinic Rossby waves generated at the eastern boundary of the
56 Arabian Sea can strengthen the eddies and contribute to their propagation (Al Saafani et al.,
57 2007). Eddies have a strong influence on the regional circulation. Mesoscale activity is re-
58 flected by high values of Eddy Kinetic Energy (Scharffenberg & Stammer, 2010) and Eddy
59 Available Potential Energy (Roulet et al., 2014), nearly reaching the values in the Antarctic
60 Circumpolar Current or the Agulhas Current. We refer the reader to Fig. 1 in L’Hégaret

61 et al. (2018) which presents the mean surface circulation in this area, and Fig. 2 in Vic et al.
 62 (2014) for a description of the mean standing eddies there, such as the Great Whirl and the
 63 dipole of Ra's Al Hadd.

64 This is the first time to our knowledge that the non-linear stability study of an isolated
 65 eddy is performed using *in situ* and satellite observed initial conditions. Here, we focus on
 66 physical processes underlying the long time evolution of the composite eddy. We address the
 67 following questions: (1) Is the composite cyclone stable in the primitive equation framework
 68 ? (2) What are the physical mechanisms involved in the destabilization of the eddy ? (3)
 69 Can the destabilization process, and the shape of the eddy after destabilization, be observed
 70 using altimetry and Argo data.

71 The paper is organized as follows. We present the composite eddy, and describe the
 72 numerical setup and tools used to study the simulation in section 2. We present the results
 73 of the simulations, and describe the diagnostics performed to analyse the possible sources of
 74 instability in section 3. We discuss sensitivity tests of our simulations in section 4. Finally,
 75 the results are discussed in section 5.

76 2. Context and methods

77 2.1. The composite eddy and its environment

78 The composite eddy was extracted using the following procedure: (1) Mesoscale eddies
 79 are detected from a $1/8^\circ$ altimetric product using the AMEDA algorithm (Le Vu et al., 2018)
 80 for the period 2000-2015. (2) A colocalization algorithm is then used to detect if an Argo
 81 float is located in or out of an eddy. (3) The background stratification of the region (Fig.
 82 1) is computed by averaging Argo profiles located outside the eddies (7885 profiles). (4) 531
 83 Argo profiles, collected inside surface-intensified Cyclonic Eddies of radius $R_D < R < 3 R_D$,
 84 are isolated. $R_D = 47$ km is the average First Baroclinic Rossby Radius of Deformation
 85 in the area (Chelton et al., 1998). (5) Density profiles are computed from Argo profiles
 86 and density anomalies are obtained by subtracting the background density in the area. (6)
 87 A dimensionless radial position $\tilde{R} = dR/R$ is computed for each profile, where dR is the
 88 distance between the center of the eddy and the position of the colocalized profile (dR), and
 89 R is the radius of the eddy. (7) The profiles are averaged depending on their value of \tilde{R} , in

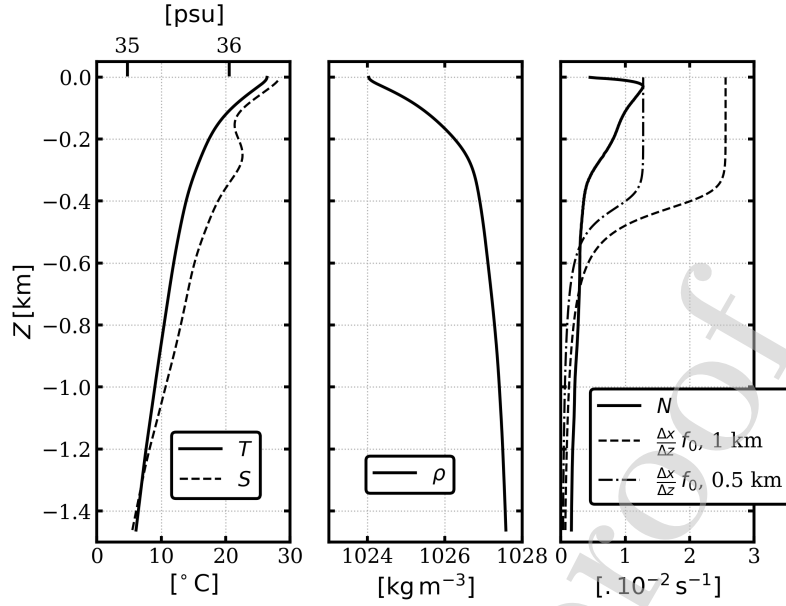


Figure 1: Background temperature (left, solid), salinity (left, dashed), density (middle) and Brunt-Väisälä frequency N (right solid) profiles, after a short period of integration. This corresponds to the stratification as found by Argo floats in the northern Arabian Sea, and used to initialize the simulations, with an additional thin surface mixed layer generated by the KPP scheme during the first days of the simulation (once created its depth is constant throughout time). The right panel shows in dashed lines the ratio $\frac{\Delta x}{\Delta z} f_0$ for two simulations, which can be compared to N ; Δx and Δz are the model grid spacings.

90 bins of width $\Delta R = 0.05$, yielding a composite vertical section of density anomaly $\tilde{\rho}(\tilde{R}, z)$. (8)
 91 For each depth, the density anomaly $\tilde{\rho}(\tilde{R}, z)$ is smoothed using a Gaussian Kernel of width
 92 0.3. (9) Finally, this composite is extrapolated into a 3D structure, by assuming azimuthal
 93 symmetry. The horizontal extent of the composite is re-dimensionalized by the mean radius
 94 of all eddies used for the computation of the composite $\langle R \rangle = 100$ km.

95 The Structure of the composite Cyclonic Eddy is thus defined in terms of a density
 96 anomaly distribution. The sum of the density anomaly of the composite and the background
 97 stratification is shown in Fig. 2. Following the same procedure, a composite structure of
 98 salinity anomaly is computed (Fig. 2b). de Marez et al. (2019) show that these structures
 99 are representative of the typical mesoscale eddies observed in the Arabian Sea. Details of
 100 the composite Cyclonic Eddy calculation and the associated validation are fully described in
 101 de Marez et al. (2019).

102 We compute the temperature anomaly field from the composite salinity and density,

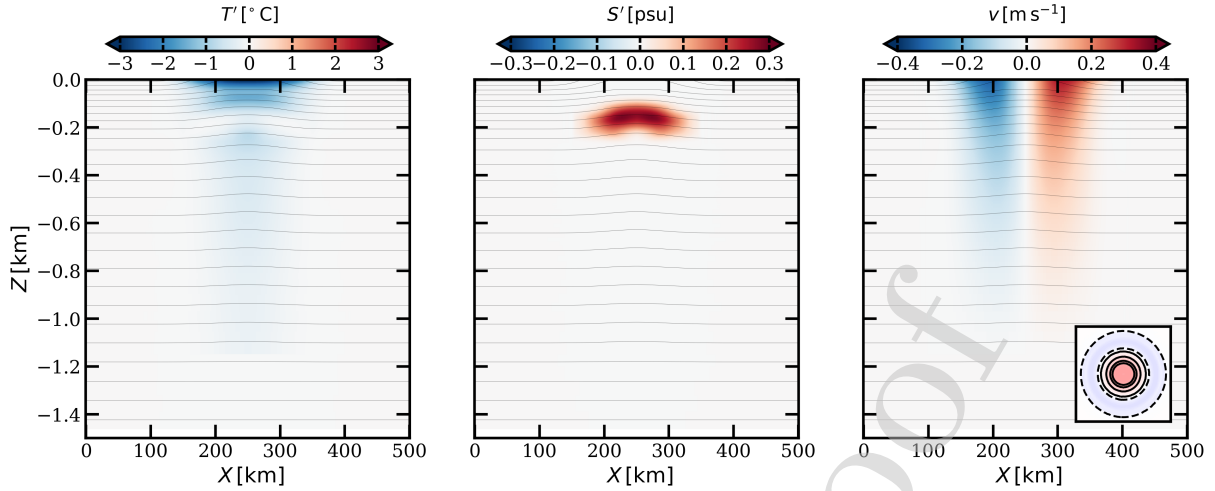


Figure 2: Vertical section at the center of the domain ($y = 250$ km) at initialization, showing the shape of the composite eddy. (left) Temperature anomaly, (middle) salinity anomaly and (right) meridional (south-north) velocity v . Iso-density contours of the composite eddy, with a spacing of 0.4 kg m^{-3} , are superposed in all panels. Insert in the right panel shows the -0.02, 0.02, 0.1, 0.2 and 0.25 dynamic Rossby number ζ/f_0 contours at the surface; the colormap in the insert is the same as in Fig. 3.

103 using the Gibbs SeaWater (GSW) Oceanographic Toolbox (McDougall & Barker, 2011),
 104 which uses the TEOS-10 equation of state for seawater (Fig. 2(a)). The background profiles
 105 shown in Fig. 1(a) are then added to the temperature and salinity anomaly fields (note
 106 that the surface mixed layer is initially not present). The velocity field is obtained *via*
 107 the cyclogeostrophic balance, following the procedure described in Penven et al. (2014), see
 108 Fig. 2(right). The numerical simulations are initialized with the temperature, salinity, and
 109 velocity fields corresponding to the composite eddy.

110 It is worth mentioning that by definition, the composite eddy has a coarse resolution.
 111 (1) On the horizontal direction: the averages of Argo-collected density profiles are made in
 112 bins of size $\Delta R = 0.05$. Once re-dimensionalized, this corresponds to a horizontal resolution
 113 of the composite eddy of 5 km. Since we perform high resolution numerical simulations, the
 114 composite eddy is interpolated on the fine grid of the simulation using a cubic-interpolation.
 115 (2) On the vertical direction: while the vertical resolution of Argo float profiles is irregular
 116 and $O(10)$ m, they were interpolated on a regularly spaced vertical grid, with a vertical
 117 spacing of 4.4 m. The composite is then linearly interpolated on the finer vertical grid of the
 118 simulation. In the simulation we will discuss, small scale variations of density and velocity

119 are of $O(< 5)$ km on the horizontal and $O(< 10)$ m on the vertical. Such small scale features
 120 thus occur at scales that the composite computation could not capture.

121 The eddy is intensified at the surface, but has a deep-reaching influence down to about
 122 1000 m depth. Its horizontal shape corresponds to a shielded vorticity monopole: a positive
 123 core of vorticity and a shield of negative vorticity (see insert in Fig. 2). Its radius, $R = 100$
 124 km, is large compared to the mean regional R_D (47 km). The Burger number, defined as
 125 $Bu = \left(\frac{R_d}{R}\right)^2$ scales as $Bu = \left(\frac{47}{100}\right)^2 \sim 0.25 < 1$. In the following, mentions to 'submesoscale'
 126 refer to features and processes occurring at scales that are small compared to R_D (*i.e.*
 127 $Bu > 1$). Typically, the fronts and vortices generated around the eddy have a typical
 128 scale of $O(< 10)$ km. They are submesoscale features. The Coriolis parameter is kept
 129 constant in the simulations (f -plane), using the regional average value (latitude of 23°N):
 130 $f_0 = 5.2 \cdot 10^{-5} \text{s}^{-1}$. The initial condition's Rossby Number is small, $Ro = \frac{U_{\max}}{f_0 R_{\max}} \sim 0.13$,
 131 with U_{\max} the maximal velocity, at R_{\max} . Thus Ro/Bu is finite, and the eddy is frontal
 132 (Stegner & Dritschel, 2000). However, it has been shown that the dynamical Rossby number
 133 $\epsilon = \zeta/f_0$, with ζ the relative vorticity is a more pertinent parameter to study geostrophic
 134 and ageostrophic dynamics in vortices (Stegner & Dritschel, 2000). In our case, $\epsilon \sim 0.3$ in
 135 the core of the eddy at initialization. Finally, the Froude number is $Fr = \frac{\epsilon}{\sqrt{Bu}} \sim 0.6$.

136 2.2. Numerical setup

137 To study the dynamics of the composite Cyclonic Eddy described in section 2.1, we
 138 perform spindown idealized simulations, with the surface fluxes set to zero, using the Coastal
 139 and Regional Ocean COMMunity model, CROCO (Shchepetkin & McWilliams, 2005). It
 140 solves the hydrostatic primitive equations (PE) for the velocity $\mathbf{u} = (u, v, w)$, temperature
 141 T , and salinity S , using a full equation of state for seawater (Shchepetkin & McWilliams,
 142 2011). The potential density referenced at the surface ρ is computed offline from T and
 143 S using the TEOS-10 equation of state for seawater. From the potential density, we also
 144 compute the Brunt-Väisälä frequency defined by

$$N = \sqrt{-\frac{g}{\rho_0} \frac{\partial \rho}{\partial z}},$$

145 with $g = 9.81 \text{ m s}^{-2}$, and ρ_0 the mean density in the domain. The simulations performed

146 integrate the PE for about 300 days on the f -plane, with a time step $dt = 120$ s, respecting
147 the Courant Friedrichs Lewy (CFL) criterion. The numerical settings are similar to previous
148 simulations performed in idealized contexts (Ménèsquen et al., 2018): horizontal advection
149 terms for tracers and momentum are discretized with fifth-order upwind advection schemes
150 (UP5); the horizontal viscosity and diffusivity are set to zero, since the UP5 scheme damps
151 dispersive errors; the vertical advection is discretized with a fourth-order centered parabolic
152 spline reconstruction (Splines scheme); the vertical closure is done by adding a small verti-
153 cal diffusion in the interior using a K-profile parameterization (KPP) (Large et al., 1994).
154 Further discussion about these parameterizations can be found in Klein et al. (2008) or
155 Ménèsquen et al. (2018).

156 The KPP-scheme generates a thin surface mixed layer during the first days of the sim-
157 ulation. The latter is not present in the background stratification at initialization because
158 it is computed as an average throughout the whole year. Once created (from $t \sim 20$ days),
159 the surface mixed layer does not evolve, and it is consistent with the surface mixed layer
160 observed in the density profiles of the Arabian Sea (except during the winter). It has a
161 vertical extension of about 30 m depth, and can be seen in Fig. 1.

162 The domain size is 500×500 km on the horizontal. Taking a flat bottom at a depth of
163 1500 m is enough because the eddy has a vertical extension of about 1000 m. We set open
164 boundary conditions at the edges of the domain. This allows the radiation of gravity waves
165 generated during the initial adjustment of the eddy. These waves are evacuated out of the
166 domain at $t = 1$ day.

167 The vertical and horizontal resolutions are chosen to accurately resolve the frontal dy-
168 namics and the forward energy cascade at the surface. The simulation has 256 vertical levels
169 stretched at the surface such that the vertical resolution is $\Delta z = 2$ m from the surface
170 to about 400 m depth. Deeper, the vertical resolution decreases, with $\Delta z \sim 60$ m at the
171 bottom. This choice was made to observe the vertical structure of the surface dynamics at
172 high resolution. The stretching of the vertical levels can be seen in Fig. 1(right). Different
173 horizontal resolutions were tested: $\Delta x = 10, 5, 2, 1,$ and 0.5 km.

174 The primary destabilization of the eddy (studied in section 3.2) depends relatively little
175 on the horizontal resolution, since it is observed in all simulations for the range of values of

176 Δx considered. The diagnosis performed to analyze this primary instability were all done
 177 on the $\Delta x = 1$ km simulation. Secondary instabilities are observed for the simulations
 178 with $\Delta x = 2, 1$ and 0.5 km. However, the time of apparition and the size of the small
 179 scale features (*e.g.* the submesoscale vortices) differ in these simulations. To ensure that the
 180 model correctly resolves the frontal processes occurring at $t > 100$ days, and to fully resolve
 181 the $O(< 10)$ km structure, the diagnosis of the secondary instabilities (see section 3.3) are
 182 performed on the $\Delta x = 0.5$ km simulation. For this one, the $\frac{\Delta x}{\Delta z}$ ratio is close to $\frac{N}{f_0}$ near
 183 the surface, see Fig. 1(right). This avoids the presence of spurious gravity waves associated
 184 with intense frontal processes, and allows a better resolution of the forward energy cascade
 185 (Snyder et al., 1993; Nadiga, 2014; Ménesguen et al., 2018).

186 For the study of the primary instability (discussed in section 3.2), the eddy is disturbed
 187 using two different methods. In the first one, the only source of perturbation is the numerical
 188 noise, due to the round-off errors at grid scale. In the second configuration we add a random
 189 noise. This noise is not spatially symmetric to avoid the dominant growth of specific az-
 190 imuthal modes. The noise is introduced as a perturbation in the initial density and velocity
 191 fields. We define the random 2D perturbation $P(x, y)$ as a sum of 5000 random Gaussian
 192 functions in the horizontal plane:

$$P(x, y) = \sum_{i=0}^{5000} A_i e^{-\frac{(x-x_0^i)^2}{2\sigma_{x,i}^2} - \frac{(y-y_0^i)^2}{2\sigma_{y,i}^2}},$$

193 where A_i , x_0^i , y_0^i , $\sigma_{x,i}$ and $\sigma_{y,i}$ are chosen randomly and independently for each i , with
 194 $-1 < A_i < 1$; $50 < x_0^i, y_0^i < 450$ km; and $5 < \sigma_{x,i}, \sigma_{y,i} < 40$ km. Then, the initial density
 195 perturbation is computed as:

$$\rho_n(x, y, z) = \rho_{n,0} P(x, y) e^{z/h_n},$$

196 with $\rho_{n,0} = 0.01 \text{ kg m}^{-3}$ and $h_n = 500$ m. The depth $h_n = 500$ m is chosen so that the vertical
 197 extent of the perturbation is similar to the vertical extent of the perturbation at $t = 7$ days in
 198 the simulation without noise. The velocity perturbation is in cyclogeostrophic balance with
 199 the ρ_n field. This avoids the radiation of gravity waves during the first days of the simulation.
 200 The values of $\rho_{n,0}$ are chosen so that the domain integral of the random perturbation's kinetic

201 energy E'_k is about 10 times larger than the kinetic energy of the perturbation at $t = 7$
 202 days in the simulation without noise. Thus, $E'_k(t = 7 \text{ days, no noise}) = 1.9 \cdot 10^7 \text{ m}^5 \text{ s}^{-2}$ and
 203 $E'_k(t = 7 \text{ days, noise}) = 29 \cdot 10^7 \text{ m}^5 \text{ s}^{-2}$. Notice that the energy of the perturbation is very
 204 weak compared to the total kinetic energy in the domain, which is about $1.8 \cdot 10^{11} \text{ m}^5 \text{ s}^{-2}$ at
 205 the initialization.

206 2.3. Definitions and tools for the study of the simulation

207 In this section, we describe the diagnostics performed. They allow us to characterize the
 208 dynamical processes involved in the destabilization of the eddy.

209 2.3.1. Different kind of instabilities

210 The different instabilities which may occur in geophysical flow can be inferred from the
 211 Potential Vorticity structure. In the primitive equation framework, the relevant definition of
 212 Potential Vorticity is the Ertel Potential Vorticity (hereafter PV). It is materially conserved
 213 in the absence of friction or diapycnal processes (Hoskins et al., 1985; Vallis, 2017), and is
 214 defined as:

$$Q = \boldsymbol{\omega} \cdot \nabla b, \quad (1)$$

215 where $b = -g \frac{\rho}{\rho_0}$ is the buoyancy, and $\boldsymbol{\omega}$ is the 3D absolute vorticity of the flow, approximated
 216 here by

$$\boldsymbol{\omega} = (-\partial_z v, \partial_z u, \zeta + f_0),$$

217 with $\zeta = (\partial_x v - \partial_y u)$ its z -component (relative vorticity hereafter). In the following, we will
 218 use the fully developed expression of the PV:

$$Q = (f_0 + \zeta) \partial_z b - (\partial_z v) (\partial_x b) + (\partial_z u) (\partial_y b). \quad (2)$$

219 An eddy with no vertical shear can be unstable with respect to barotropic (BT) instability.
 220 A necessary condition is that its radial gradient of PV, $\partial_r Q$, changes sign on the horizontal
 221 (*i.e.* within a layer of constant density).

222 Also, an eddy can be unstable with respect to baroclinic (BC) instability. The necessary
 223 condition is that its radial gradient of PV, $\partial_r Q$, changes sign on the vertical (*i.e.* between
 224 different layers). This latter change of sign can occur in the fluid interior (Phillips-type BC
 225 instability). If isopycnals outcrop, surface density gradients generate PV sheets (Bretherton,
 226 1966) which, in turn, induce sharp PV gradients localized at the surface (Morel et al., 2006).
 227 The change of sign of the PV gradient can thus also occur between the surface and the
 228 interior (Charney-type BC instability), or between two sheet-type PV anomalies, at the
 229 surface and at the bottom (Eady-type instability) (Hoskins et al., 1985). In the mixed
 230 layer, the conditions for BC instability are changed and the theory described above is rather
 231 unsatisfactory. We refer the reader to Young & Chen (1995) for further description.

232 In geophysical flows, symmetric instability (SI) may also occur when the product of plan-
 233 etary vorticity and potential vorticity becomes negative ($fQ < 0$) (Fjørtoft, 1950; Hoskins,
 234 1974; Bell, 2018). This is an overturning instability occurring in baroclinic currents, which
 235 results from an imbalance between the pressure gradients and the inertial forces (Thomas
 236 et al., 2013). It occurs where the dynamic is frontal and where the PV of the flow is negative
 237 (in the Northern hemisphere) because of the second and/or the third term of its expression
 238 (eq. (2)). Following Thomas et al. (2013), a necessary condition for SI instability can be
 239 derived. First, we define the balanced Richardson number of the flow

$$240 \quad Ri = \frac{f_0^2 N^2}{|\nabla b|^2}, \quad (3)$$

and the critical Richardson number

$$241 \quad Ri_c = \frac{f_0}{\zeta_g}, \quad (4)$$

where ζ_g is the absolute vorticity of the geostrophic flow such as

$$242 \quad \zeta_g = f_0 + (\partial_x v_g - \partial_y u_g), \quad (5)$$

243 where u_g and v_g are the zonal and meridional components of the geostrophic velocity in the
 244 simulation. PV of a geostrophic flow is negative when $Ri < Ri_c$. When this condition is
 met, SI can develop.

245 *2.3.2. Energy transfer terms*

246 The nature of the instabilities occurring in the flow may be investigated by studying the
 247 energy transfers. We assume that the flow may be decomposed as $\mathbf{u} = \langle \mathbf{u} \rangle + \mathbf{u}'$, where the
 248 brackets $\langle \cdot \rangle$ denotes a mean state and the prime $'$ is the perturbation relative to this mean
 249 state. First, the transfer from the mean kinetic energy (MKE) to the kinetic energy of the
 250 perturbation (EKE) may be expressed as:

$$(MKE \rightarrow EKE) = HRS + VRS, \quad (6)$$

where

$$HRS = -\langle u'^2 \rangle \partial_x \langle u \rangle - \langle u'v' \rangle \partial_y \langle u \rangle - \langle v'^2 \rangle \partial_y \langle v \rangle - \langle u'v' \rangle \partial_x \langle v \rangle \quad (7)$$

251 is the contribution from the Horizontal Reynolds Stress, and

$$VRS = -\langle u'w' \rangle \partial_z \langle u \rangle - \langle v'w' \rangle \partial_z \langle v \rangle \quad (8)$$

252 is the contribution of the Vertical Reynolds Stress. Note that eq. (6) is obtained by integrat-
 253 ing over the whole domain. Thus, formally, there are transport terms at the boundaries of
 254 the domain. In our simulations, these terms are null. Second, the transfer from the Potential
 255 Energy of the perturbation to the EKE is the Vertical Buoyancy Flux:

$$VBF = \langle w'b' \rangle. \quad (9)$$

256 The predominance of HRS, VRS, or VBF (> 0) in a region indicates a BT, Kelvin-
 257 Helmholtz type, or a BC instability respectively. More details on this decomposition and
 258 applications to the case of instabilities in the path of the Gulf Stream can be found in
 259 Gula et al. (2015, 2016). In our study, we use this decomposition to study (1) the primary
 260 instability of the eddy (Fig. 7 and A.17), and (2) the secondary instabilities occurring in the
 261 fronts around the eddy (Fig. A.18 and A.19).

262 In the first case, the mean flow defined by the variables $\langle u, v, w, b \rangle$ is assumed to be
 263 the initial state of the eddy. This choice allows to study the transfers of energy from the
 264 axisymmetric eddy to the perturbation. The perturbations u', v', w', b' are computed with
 265 respect to this initial state. Then, all time averaged products $\langle \cdot \cdot' \rangle$ are performed using a

266 rolling time-mean average over a 1-month window (the growth time of the primary instability;
267 see the following section).

268 In the second case, where we study the energy transfer to small scale structures (fronts
269 and submesoscale vortices) rotating around the eddy, we project the variables in the frame of
270 reference of the perturbation (rotating at a constant azimuthal velocity). $\langle \cdot \rangle$ is defined as a
271 rolling time-mean average over a 10-days period in the rotating frame (the typical timescale
272 of destabilization of the fronts). Perturbations \cdot' are computed with respect to this rolling
273 time-mean average.

274 2.3.3. Normal mode decomposition

275 Perturbations are projected into azimuthal normal modes (Gent & McWilliams, 1986).
276 Hereafter, the primed quantities denote the perturbation of A with respect to its initial
277 value, such as

$$A'(t, x, y, z) = A(t, x, y, z) - A(t = 0, x, y, z).$$

278 Also, A^m is the decomposition of A into azimuthal normal modes. This decomposition is
279 defined as follows:

$$A(t, r, \theta) = \sum_{m=0}^{m=\infty} A^m(t, r, \theta), \quad (10)$$

280 in the polar coordinates referenced at the center of the eddy (r, θ) , where

$$A^m(t, r, \theta) = a_m(t, r) \cos(m\theta + \phi_m(t, r)). \quad (11)$$

281 m is the azimuthal wavenumber and a_m and ϕ_m the amplitude and the phase of the mode,
282 respectively. The phase velocity of the perturbation for the mode m is:

$$c_\phi^m(t, r) = \partial_t \phi_m(t, r). \quad (12)$$

283 The kinetic energy of the perturbation is defined as:

$$E'_k(t) = \frac{1}{2} \iiint dx dy dz (u_r'^2 + u_\theta'^2), \quad (13)$$

284 where u'_r and u'_θ are the radial and azimuthal velocity perturbations. Similarly, the kinetic
 285 energy of the mode m perturbation is:

$$E'_k{}^m(t) = \frac{1}{2} \iiint dx dy dz \left((u'_r{}^m)^2 + (u'_\theta{}^m)^2 \right). \quad (14)$$

286 In these two expressions, the integrals are performed over the whole domain of the simulation.
 287 Using exponential notation, time evolution of normal mode perturbation velocity reads:

$$\mathbf{u}'^m(t) = \mathbf{u}'_0{}^m e^{im(\theta-ct)}, \quad (15)$$

288 which yields an exponential form for the the energy growth:

$$E'_k{}^m(t) = E'_{k,0}{}^m e^{2\sigma t}. \quad (16)$$

289 Where $E'_{k,0}{}^m$ is the initial perturbation and $\sigma = Re(-imc)$ is the growth rate. In our case,
 290 we choose to set $E'_{k,0}{}^m = E'_k{}^m(t = 7 \text{ days})$. This reference is chosen as close as possible from
 291 the beginning of the simulation, without having problem with division by zero when com-
 292 puting the growth time. In the simulations, perturbation growth rates are inferred from the
 293 amplification factor (λ):

$$\lambda_{E'_k{}^m} = \frac{E'_k{}^m(t)}{E'_{k,0}{}^m}. \quad (17)$$

294 The growth time is defined as $\tau_{E'_k{}^m} = \sigma_{E'_k{}^m}^{-1}$ with

$$\sigma_{E'_k{}^m} = \frac{1}{2t} \ln(\lambda_{E'_k{}^m}). \quad (18)$$

295 Then,

$$\tau_{E'_k{}^m}(t) = -2t \ln\left(\frac{E'_k{}^m(t)}{E'_{k,0}{}^m}\right). \quad (19)$$

296 When $\tau_{E'_k{}^m}$ is small, the growth of the perturbation is rapid.

297 2.3.4. Critical level computation

298 The position of the critical level for azimuthal mode 2 at the surface is found by seeking
 299 the position where the phase speed of the mode 2 perturbations is equal to the angular

300 velocity of the eddy. This latter is here an azimuthal average of the azimuthal velocity u_θ of
 301 the eddy. At each time we thus obtain the position of the critical level for the mode 2. We
 302 then average this position during the period $t = [50 : 70]$ days, to obtain the typical position
 303 of the critical level during the linear phase of the perturbation.

304 The energy of normal modes can concentrate within the critical level, as further described
 305 in Nguyen et al. (2012) or Riedinger & Gilbert (2014). In our study, we show that the
 306 presence of the critical level for mode 2 induces an intense stretching of the flow S . The
 307 latter is defined as the sum of the strain and the shear:

$$S = \underbrace{\partial_x u - \partial_y v}_{\text{Strain}} + \underbrace{\partial_x v + \partial_y u}_{\text{Shear}}.$$

308 It describes the tendency of the water parcels to be deformed by the ambient flow. Buoyancy
 309 gradients are steepened by this stretching. To describe the evolution of buoyancy gradients,
 310 we use the frontogenesis function F associated with the buoyancy. It is calculated using its
 311 standard definition as follows (Hoskins, 1982):

$$F(\mathbf{u}, b) = \partial_x u (\partial_x b)^2 + (\partial_x v + \partial_y u) \partial_x b \partial_y b + \partial_y v (\partial_y b)^2. \quad (20)$$

312 The opposite of F indicates the tendency of the buoyancy gradients to steepen:

$$-F(\mathbf{u}, b) = \frac{d}{dt} |\nabla b|^2.$$

313 3. Results

314 3.1. Overall course of the simulation

315 We present here the overall course of the simulation, and we separate the different stages
 316 of the eddy evolution that we will discuss in the following sections.

317 Fig. 3 shows the evolution of relative vorticity after 70, 100, 180, and 300 days of
 318 simulation (panels (a), (b), (c), and (d) respectively). During the first part of the simulation
 319 (for $0 < t < 100$ days), a mixed BT/BC instability causes the eddy core to deform as spiral
 320 arms grow around it, see Fig. 3(a). Azimuthal mode 2 dominates, and the growth rate of the
 321 perturbation is roughly constant. The BC component of the instability leads to an intense

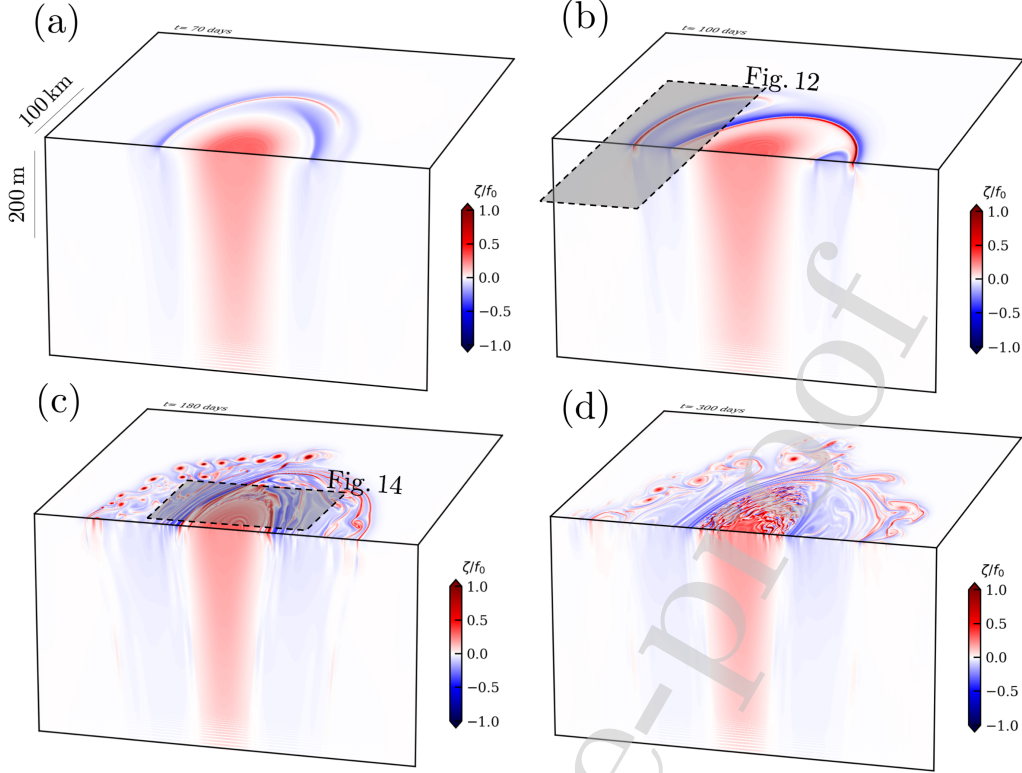


Figure 3: Snapshots of the normalized relative vorticity ζ/f_0 at $t = 70, 100, 180$ and 300 days in the $\Delta x = 0.5$ km resolution simulation. Notice that the z -scale is very stretched to show the depth extension of the near-surface dynamics, see horizontal and vertical scalebars in panel (a). Gray rectangles in (b) and (c) show the regions studied in Fig. 12 and 14.

322 frontogenesis at the edge of the eddy and in the spiral arms, see Fig. 3(b). Then, secondary
 323 instabilities occur in the surface mixed layer, see Fig. 3(c). In particular, shear instability
 324 develops in the spiral arms, generating series of small vortices of $O(10)$ km. The steepening
 325 of buoyancy gradients at the edge of the eddy also induces diapycnal mixing. This causes
 326 PV to change sign and yields SI. The latter erodes the edge of the eddy by creating fine scale
 327 structures of $O(2)$ km which are then ejected far away from the eddy, see Fig. 3(d). While
 328 secondary instabilities occur, the deepest part of the eddy ($z < -50$ m) remains a mesoscale
 329 tripole. It remains coherent during the last 6 months of the simulation. In subsection 3.2,
 330 we describe the evolution of the cyclone from $t = 0$ to $t \sim 100$ days. Then, we present the
 331 secondary instabilities which occur in the surface mixed layer in subsection 3.3.

332 3.2. Primary instability: the monopole becomes a tripole

333 3.2.1. Growth of normal modes

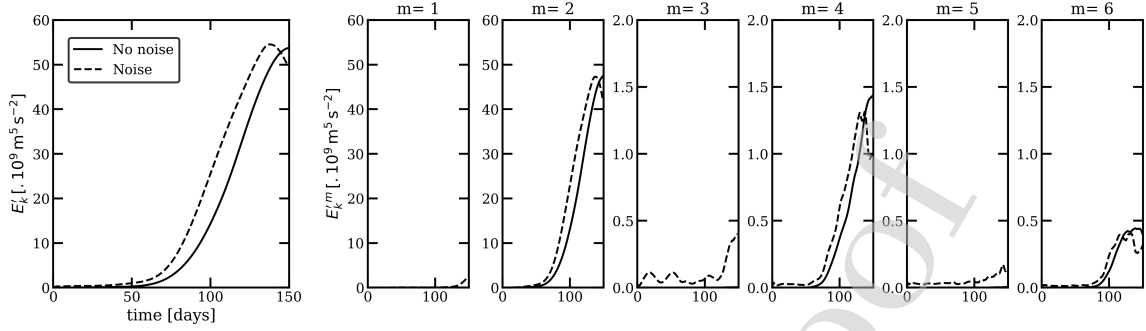


Figure 4: Time evolution of the perturbation kinetic energy E'_k , for the simulation with random noise (dashed line) and without noise (solid line). The left panel shows the total kinetic energy of the perturbation (for all modes). The panels on the right show the kinetic energy of the first six azimuthal normal modes. Notice that the vertical scale for the perturbation energy is not the same for plots corresponding to $m > 2$.

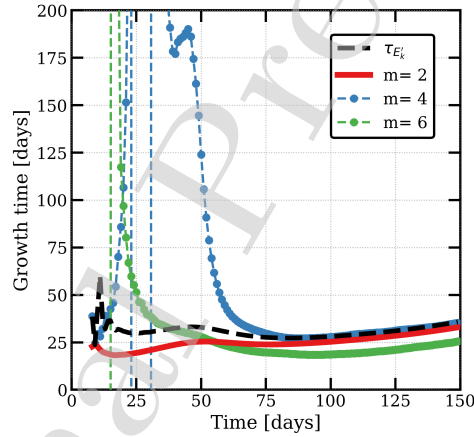


Figure 5: Time evolution of the growth time (in days) of the total kinetic energy of the perturbation $\tau_{E'_k}$ (dashed line); and evolution of the growth time of the normal modes $\tau_{E'_k^m}$ for mode 2 (red), 4 (blue) and 6 (green), for the simulation without noise.

334 During the first 100 days of the simulation, the eddy destabilizes, with a domination of
 335 even azimuthal modes. To study the evolution of the perturbation, we compute its total
 336 kinetic energy at all times following eq. (13), and for each azimuthal mode following eq.
 337 (14), see (Fig. 4). The simulation without initial noise is compared to the simulation with
 338 a random noise.

339 No difference is discernible in terms of growth of the perturbation between the two cases,
 340 showing that the structure is intrinsically unstable regardless of the initial perturbations.
 341 The total kinetic energy of the perturbation increases slowly at the first days of simulations.
 342 It then grows exponentially after $t \sim 50$ days, and tends to a plateau at $t \sim 150$ days.

343 The even modes have similar growth rates in the two simulations. In particular, the
 344 azimuthal mode 2 dominates, with values of energy close to the total energy of the pertur-
 345 bation. In the simulation where initial conditions are initially perturbed by a random noise,
 346 odd azimuthal modes are present at the initialization. These modes do not grow during the
 347 primary stage of the instability, meaning that they are stable. The processes involved in the
 348 primary destabilization of the eddy are well captured by the simulation without noise. In
 349 the following, we focus on the simulations performed without random noise.

350 The growth time of the perturbation is computed using eq. (19) for the total kinetic
 351 energy of the perturbation, for modes 2, 4 and 6 (Fig. 5). The growth time of the total
 352 kinetic energy of the perturbation (*i.e* for all modes) is, on average, around 30 days. From
 353 the beginning of the simulation, the growth time of mode 2 is almost equal to the growth
 354 time of the total perturbation, confirming that the instability is controlled by mode 2. Its
 355 growth time is roughly constant between day 50 and day 90, indicating that during this
 356 stage, mode 2 growth is exponential and evolves independently of the other modes (Gent &
 357 McWilliams, 1986).

358 At the beginning of the simulation, transient perturbations occur in the core of the eddy,
 359 mostly stemming from the initial adjustment of the eddy. They are evanescent and rapidly
 360 decay (Riedinger & Gilbert, 2014). However, during the first 20 days, their energy has similar
 361 magnitude to that of the unstable mode 2. They are believed to trigger mode 2. We next
 362 focus on the evolution of mode 2 since it dominates the instability. One can mention that for
 363 higher modes, nonlinear interactions most likely occur; their growth rates are not constant
 364 and have a similar evolution between each other.

365 3.2.2. *Instability mechanism*

366 The radial PV gradient $\partial_r Q$ is shown in Fig. 6. The horizontal change of sign of $\partial_r Q$
 367 in the whole water column indicates that the structure may be barotropically unstable.

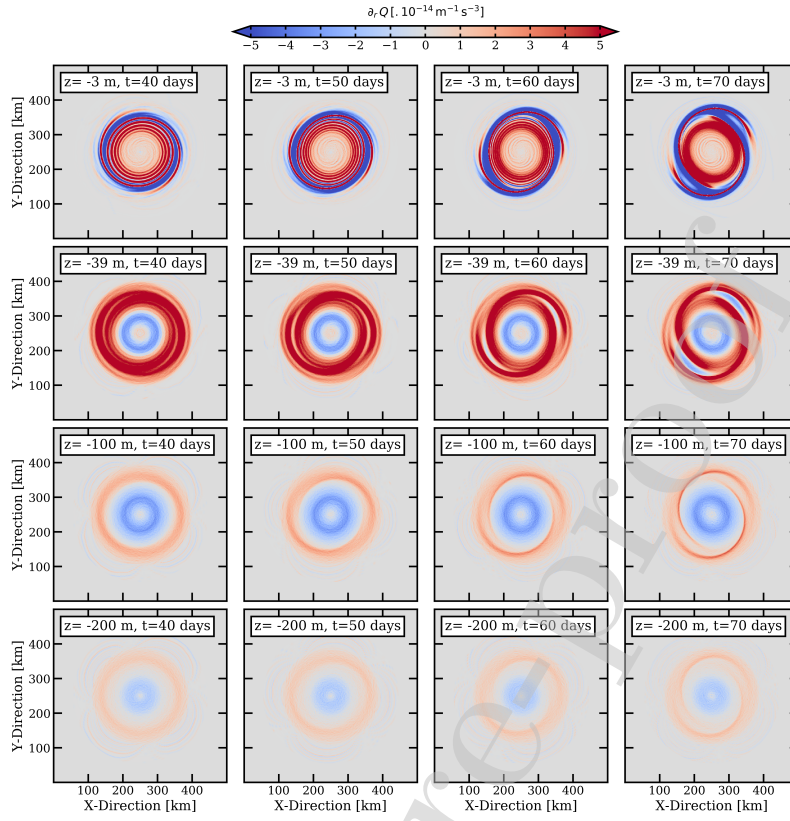


Figure 6: Radial derivative of the PV at $t = 40, 50, 60,$ and 70 days (from left to right), at $3, 39, 100$ and 200 m depth (from top to bottom).

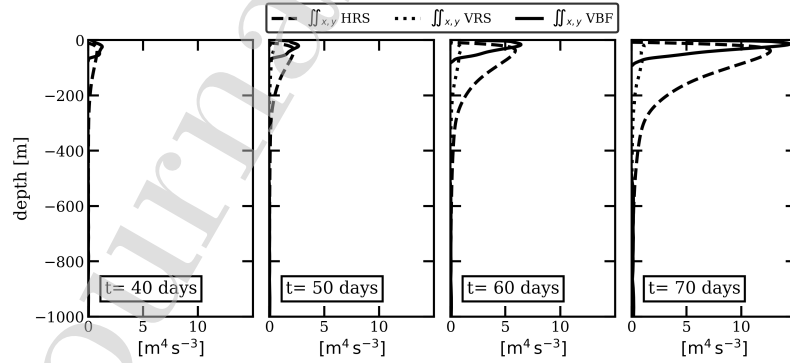


Figure 7: Profiles of energy transfer terms integrated on the horizontal at $t = 40, 50, 60,$ and 70 days (from left to right). HRS, VRS, and VBF stand for Horizontal Reynolds Stress, Vertical Reynolds Stress, and Vertical Buoyancy Flux.

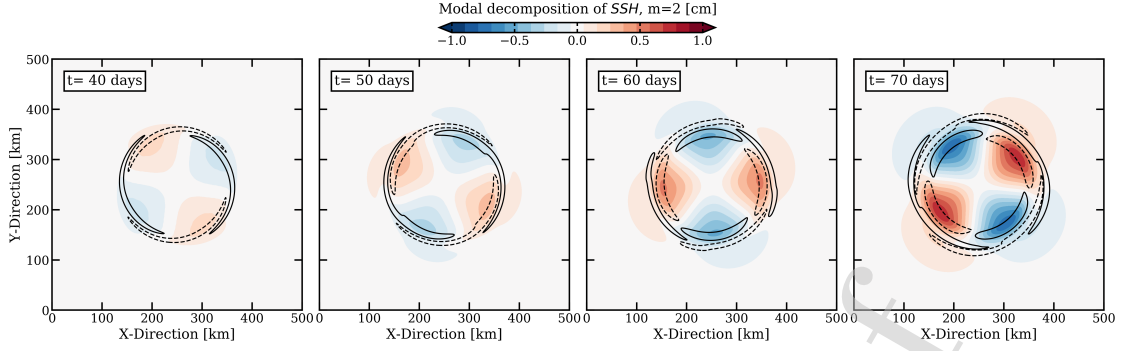


Figure 8: Mode 2 of the SSH during the linear phase of the perturbation, at $t = 40, 50, 60,$ and 70 days. It shows the counter-clockwise rotation of the eddy Rossby Wave (VRW) around the eddy. This wave rotates of about a quarter turn in 30 days. We superposed the contours (± 0.02) of the mode 2 perturbation of normalized relative vorticity at the surface $\zeta^{m=2}/f_0$.

368 At the center of the eddy, isopycnals outcrop (not shown), thus creating regions of high
 369 PV. Intersection lines between the surface and outcropping isopycnals are places of strong
 370 horizontal PV gradients. It can be seen in Fig. 6 at $z = -3$ m. This leads to a change
 371 of sign of $\partial_r Q$ in the vertical direction, between the surface and the interior PV gradients:
 372 the necessary condition for a Charney-type BC instability. The general stability conditions
 373 described by Pedlosky (1964); Eliassen (1983); Hoskins et al. (1985); Ripa (1991), stating
 374 that

$$(u_\theta - \alpha)\partial_r Q < 0$$

375 and

$$N^2(\delta z_\rho)^2 > (u_\theta - \alpha)^2$$

376 in the whole domain, for any α , with δz_ρ the vertical displacement of isopycnals, are also
 377 not respected in the whole domain (not shown). All necessary conditions for BT or BC
 378 instabilities to occur are thus met. Such mixed BT/BC instabilities have already been
 379 observed in high resolution numerical simulations, in particular in the case of Meddy-like
 380 eddies, see for instance Ménesguen et al. (2018).

381 Here, while the instability is mainly BT, it is strengthened by a small baroclinic mode
 382 near the surface. The energy transfer terms (HRS, VRS and VBF) integrated along the

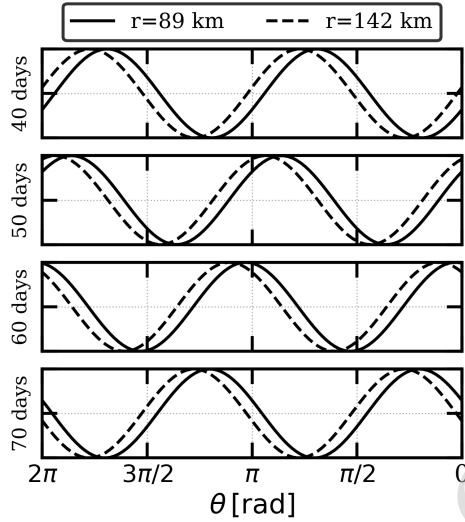


Figure 9: Comparison between the phase of the outer VRW and the inner VRW, in the mode 2 component of the SSH. Solid (resp. dashed) black lines shows cosinus with the phase of the mode 2 VRW at $r=89$ km (resp. 142 km) for the same times as in Fig. 8 (from top to bottom).

383 horizontal directions are shown in Fig. 7. During the growth of the instability, HRS and
 384 VBF dominate, confirming that the instability is both BT and BC as predicted by the
 385 structure of the PV profile (Fig. 6). The HRS term is deep reaching and shows that the
 386 BT instability dominates the formation of the tripole. This instability penetrates deeply,
 387 and drives the formation of the tripole in the whole water column during the first 100 days
 388 of the simulation. The structure of the tripole at depth can be seen in Fig. 3(d), with a
 389 strong barotropic component of the positive and negative poles, and an outer ring of positive
 390 vorticity (*i.e.* the spiral arms). The VBF term is maximum near the surface, at the interface
 391 between the SML and the interior. This suggests that the instability is intensified by a
 392 BC component at the surface. Maps of vertically integrated transfer terms are presented
 393 in Appendix A, in Fig. A.17. In summary, together Fig. 7 and A.17 show that the BC
 394 instability participates in forming intense spiral arms in the SML, while the BT instability
 395 leads to the deformation of the core of the eddy.

396 To understand the destabilization of the eddy, one can notice that the propagation of
 397 the unstable mode 2 is that of a Vortex Rossby wave (VRW), rotating around the eddy.
 398 This wave is supported by the radial gradient of PV of the eddy. This process is similar
 399 to planetary Rossby waves in the ocean, supported by the meridional PV gradient induced

400 by the β -effect. The signature of the VRW in the simulation can be seen in the mode 2
 401 component of the SSH. The VRW rotates about a quarter turn in 30 days (Fig. 8) giving
 402 $c_{VRW} = 0.05 \text{ rad days}^{-1}$. This value is consistent with the estimation of the phase speed of a
 403 baroclinic perturbation rotating around a unstable barotropic eddy in the quasi-geostrophic
 404 framework (see Appendix B). The mode 2 VRW exhibits different patterns depending on
 405 its position from the center of the eddy, see Fig. 9. It can be separated into two VRW
 406 rotating around the eddy at the same speed: an outer VRW (oVRW) at $r > 100 \text{ km}$, and
 407 an inner VRW (iVRW) at $r < 100 \text{ km}$. They are phase shifted. The oVRW is in advance
 408 compared to the iVRW. As these two waves interact, they amplify mutually, and the total
 409 perturbation rotating around the eddy grows (Flierl, 1988).

410 3.2.3. Critical level consequences

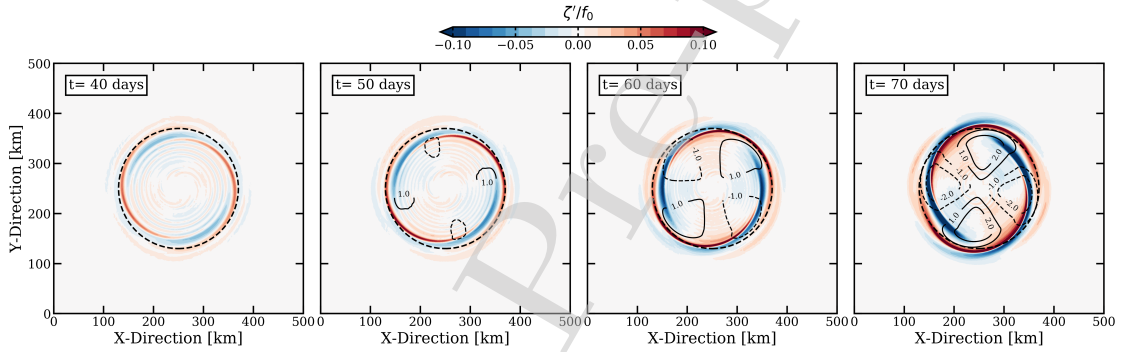


Figure 10: Time evolution of the perturbation of relative vorticity at the surface, at $t = 40, 50, 60,$ and 70 days. Contours of the mode 2 component of the surface radial velocity $u_r^{m=2}$ for the values $-2, -1, 1,$ and 2 km day^{-1} are superposed. It shows that the perturbation of the radial velocity is nearly in phase quadrature with the vorticity. The position of the critical level for the mode 2 is shown with the dashed black circle, at $r = 120 \text{ km}$.

411 The presence of a critical level (CL) for mode 2 leads to an important frontogenesis at the
 412 edge of the eddy and in the spiral arms. As discussed in Nguyen et al. (2012), the azimuthal
 413 speed of the VRW which carry the perturbation is small compared to the maximal swirl
 414 angular velocity of the eddy. The critical level is thus located far from the center of the
 415 eddy, where its swirl velocity decreases outward (here on average at $r = 120 \text{ km}$). This value
 416 was obtained during the linear stage, following the method described in section 2.3.4. At
 417 the initial stage of the instability, for $t \sim 40\text{-}60$ days, the perturbation is wrapped around

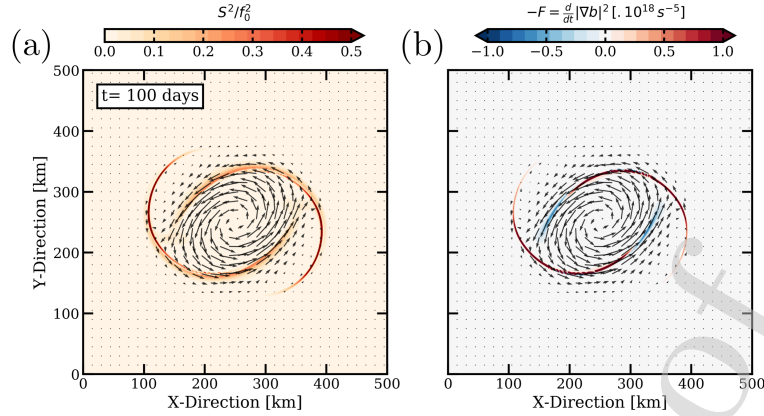


Figure 11: Frontogenesis mechanism at $t = 100$ days. (a) Stretching at the surface normalized by the Coriolis frequency, and (b) opposite of the Frontogenesis function ($-F$) at the surface, reflecting the steepening of buoyancy gradients. The horizontal velocity at the surface is superposed in both panels.

418 the eddy in the form of long vorticity filaments near the critical level position (Fig. 10). At
 419 this time, the eddy is still mostly circular, since the radial velocity is weak. Then, the mode
 420 2 component of radial velocity u_r' grows. It reaches a value of several kilometer per day
 421 (see Fig. 10). Since it is nearly in phase quadrature with the vorticity, this radial velocity
 422 perturbation leads to the ellipticization of the eddy, and to the creation of spiral arms around
 423 the eddy.

424 At $t \sim 100$ days, after the linear stage of the mode 2 perturbation, the eddy becomes
 425 elliptical, and two spiral arms form. These arms are very thin since they were initially
 426 elongated around the CL. Stretching dominates the flow at the edge of the eddy and in the
 427 spiral arms (Fig. 11 (a)). The flow generated by the primary instability thus forces the
 428 gradients to steepen, in particular, the buoyancy gradients. The frontogenesis function F
 429 associated with the buoyancy is computed at the surface and it is shown in Fig. 11(b).
 430 In the spiral arms and at the edges of the eddy, $-F$ is large. It reflects the steepening of
 431 the buoyancy gradients with time. Thus, the flow follows a frontal dynamic in these areas:
 432 the isopycnals outcrop and are very steep. Furthermore, the dynamical Rossby number
 433 $\epsilon = \zeta/f_0$ becomes locally larger than 1 (see Fig. 3), indicating that the circulation is
 434 mostly ageostrophic in these regions (Stegner & Dritschel, 2000). These observations are in
 435 agreement with the results of Nguyen et al. (2012) and Hua et al. (2013), who show that

436 density gradients are enhanced at critical levels.

437 3.3. Secondary instabilities and their impact on small scale structures

438 The primary BT/BC instability saturates at $t \sim 120$ days, after the initial monopole
 439 has evolved into a stable tripole; this tripole remains stable during the next 6 months of
 440 the simulation below the surface mixed layer. Inside the surface mixed layer, the intense
 441 frontogenesis leads to sharp fronts near the surface.

442 The small scale structures located in the surface mixed layer follow a Surface Quasi
 443 Geostrophic (SQG) dynamic. Because they have a small horizontal size, these surface fea-
 444 tures have a small vertical influence. Indeed, in the framework of the SQG model, following
 445 Isern-Fontanet et al. (2008), the streamfunction is $\Psi_{SQG} \propto e^{\frac{N_0 k}{f_0} z}$, where k is the horizontal
 446 wavenumber at the surface. The smaller horizontal scales decay in the vertical faster than
 447 larger ones. The vertical extension of surface structures scales as:

$$L_z = \frac{f_0 L}{2\pi N_0 f_0},$$

448 where L is the horizontal size of surface features and $N_0 \sim 10^{-2} \text{ s}^{-1}$ the typical stratification,
 449 leading to

$$L_z \sim 10^{-3} L.$$

450 In our case, filaments and submesoscale vortices which evolve at the surface have a size of
 451 $O(< 10)$ km. Therefore, they have a vertical influence over $O(< 10)$ m. This vertical scale
 452 applies to the stratified fluid below the surface mixed layer. It shows that the submesoscale
 453 is largely confined to the mixed layer, as it can be seen in Fig. 3 at $t \geq 100$ days.

454 3.3.1. Barotropic instability at the surface as a source of submesoscale

455 In the spiral arms, the steep PV gradients create favorable conditions for BT instability.
 456 BT instability occurs in a thin surface mixed layer in which the flow is confined, and leads to
 457 the destabilization of the spiral arms at $t \sim 110$ days. A mean PV section of a spiral arm (Fig.
 458 12(b)) was computed by averaging 10 vertical sections at $t = 110$ days (Fig. 12(a)). The
 459 PV anomaly of the spiral arm is confined in the upper 10 m. The cross-filament derivative

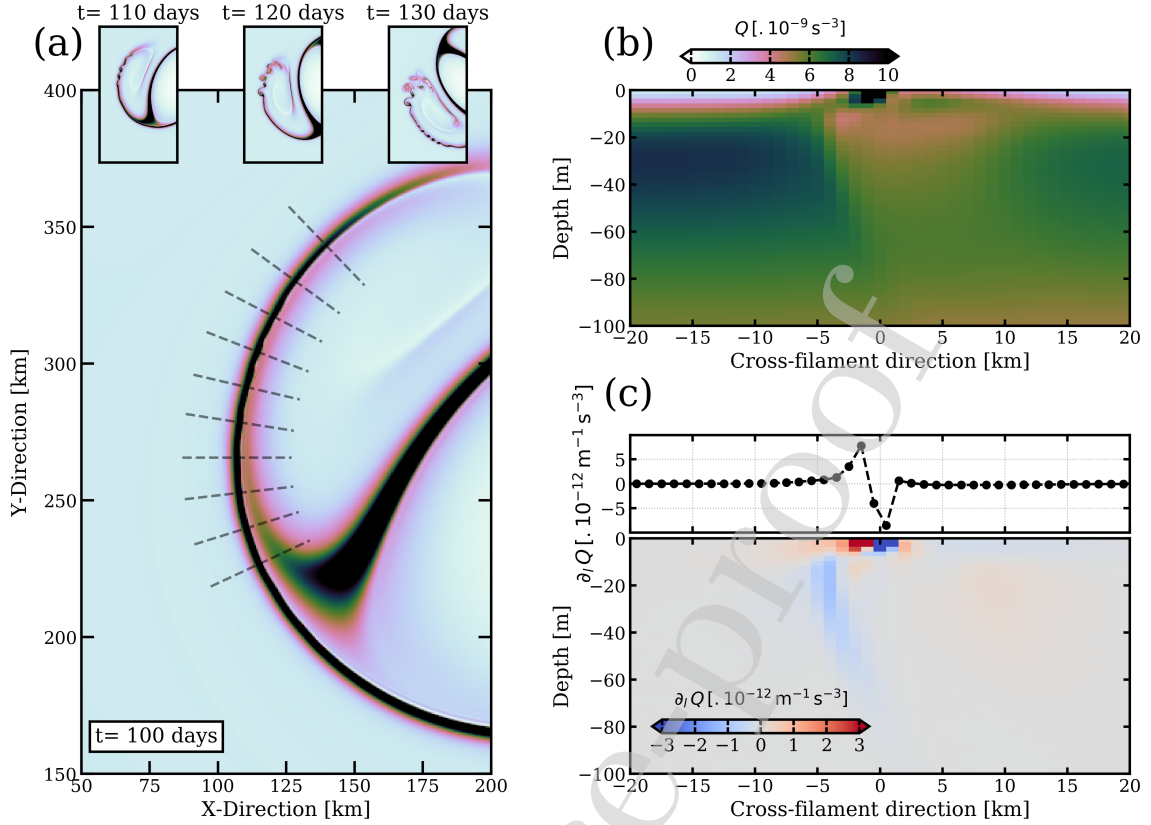


Figure 12: (a) Snapshot of surface PV, at $t = 100$ days before the BT instability in the spiral arms. The domain shown is the western part of the eddy. Inserts present snapshots of surface PV at $t = 110$, 120 and 130 days. (b) Mean vertical section of PV computed using 10 sections perpendicular to the spiral arm at $t = 100$ days (their position is indicated in (a) by the grey dashed lines). The colormap of (a) and (b) is the same. (c) Derivative of the PV along the axis of the section, at the surface (top), and in the first 100 meters (bottom).

460 of the PV ($\partial_t Q$) changes sign along the section, signature of BT instability (Fig. 12(c)).
 461 Small ambient perturbations trigger instability, forming a row of small vortices of positive
 462 relative vorticity. The first ones appear at $t \sim 110$ days, at the tip of the arms. At $t \sim 130$
 463 days, the whole arms destabilize (Fig. 12(a)), and evolve into a row of submesoscale vortices
 464 surrounding the main eddy (Fig. 3(c)). A few of the satellite vortices remain coherent for
 465 about 6 months. The energy transfer terms in the spiral arm are shown in Fig. A.18, see the
 466 calculation method in section 2.3.2. It shows a strong signature of positive HRS in the arm
 467 when it becomes unstable, confirming that destabilization is due to a purely BT instability
 468 in the surface mixed layer. These observations show that BT instability of the spiral arms of

469 a large unstable eddy is an efficient mechanism for the formation of submesoscale vortices.

470 To investigate the possibility of secondary instability to be triggered by grid-scale numer-
 471 ical noise, a sensitivity test was performed, adding a random noise in the simulation at $t =$
 472 90 days. In this case, the arms destabilize slightly earlier, at $t = 105$ days, but in a similar
 473 way, still forming a row of small vortices. As for the primary instability of the vortex, the
 474 vorticity arms are intrinsically unstable.

475 At the edge of the eddy core, the cross-front PV gradient changes sign on the horizontal
 476 as well as on the vertical (not shown). Thus, the edge of the eddy is unstable with respect to
 477 a mixed BT/BC instability. Because the PV gradients are weaker, growth rates are slower
 478 than observed in the arms. However, at $t \sim 150$ days, the small vortices generated around
 479 the eddy start to merge with the vortex edge, triggering instability. This is confirmed by
 480 large values of HRS and VBF at the edge, where the small eddies interact with the larger
 481 one (Fig. A.19). Then, a short wavelength elliptical VRW propagates around the eddy (see
 482 the deformation of the eddy's edge in Fig. 3(c).

483 3.3.2. Evidence of symmetric instability at the edge of the eddy

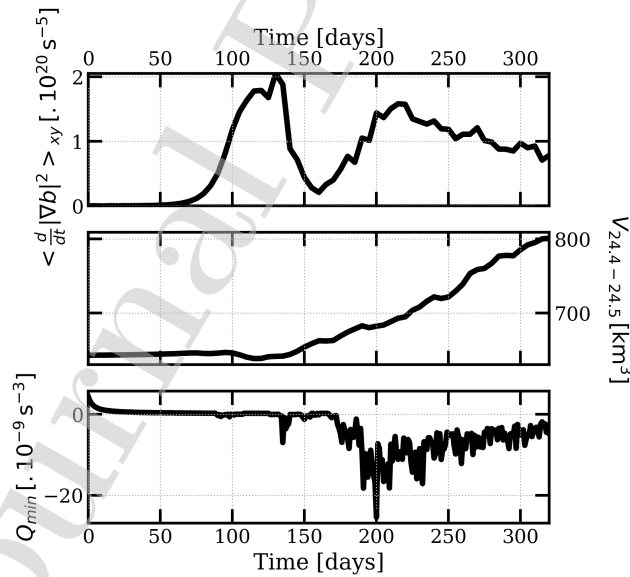


Figure 13: Time evolution of (top) the average of $-F(\mathbf{u}, b) = \frac{d}{dt} |\nabla b|^2$ at the surface, (middle) the volume between the $\rho = 1024.4 \text{ kg m}^{-3}$ and the $\rho = 1024.5 \text{ kg m}^{-3}$ isopycnals, and (bottom) the minimum of PV in the domain.

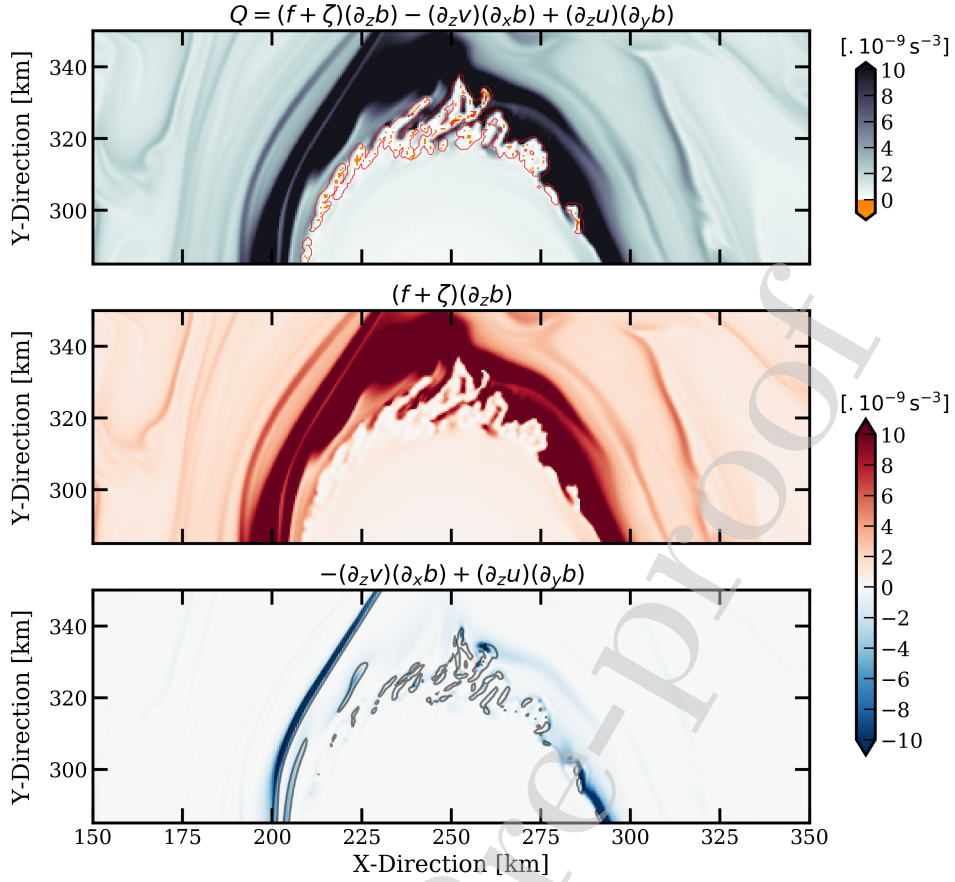


Figure 14: Decomposition of the PV at $t = 180$ days, at the southern part of the eddy. (top) PV at the surface; the yellow indicates places where the PV is negative, and the red lines indicate regions where the criterion for SI to occur $Ri < Ri_c$ is respected. (middle) First term of the PV. (bottom) Second and third terms of the PV; contours of $-F = 10^{-18} \text{ s}^{-5}$ are superposed as grey thin lines.

484 A second phase of frontogenesis is triggered as the small scale VRW deforms the front
 485 at the edge of the eddy through intense stretching. Time evolution of the mean $-F$ at the
 486 surface is shown in Fig. 13(top). At $t = 160$ days, steepening of the buoyancy gradient
 487 starts to increase for a second time. The second and third terms of the PV (in eq. (2))
 488 become very intense locally, see *e.g.* Fig. 14(bottom). Indeed, the variations of velocity
 489 are localized at the surface, and variations of buoyancy occur at scales of $O(1)$ km. These
 490 terms are negative and of the same order of magnitude as the first term of the PV, see Fig.
 491 14(middle), leading to a PV close to zero where the fronts are sharp (Fig. 14(top)).

492 The horizontal buoyancy variations occur at very fine scales (see the contours of $-F$
 493 at $t = 180$ days on Fig. 14(bottom)). The circulation at the edge of the eddy becomes

494 strongly ageostrophic from $t \sim 160$ days, leading to diapycnal mixing at the edge of the
 495 eddy. The latter acts in decreasing stratification, leading to a PV sign change. In our model,
 496 since diapycnal mixing is parameterized through the KPP-scheme, we do not attempt to
 497 characterize it, and rather focus our attention on the dynamical processes resulting of the
 498 diapycnal mixing.

499 A first explanation for the decrease of the PV due to diapycnal mixing can be found by
 500 introducing changes of buoyancy in the expression of the PV. We present in Appendix C
 501 how the PV sign can change if it is initially close to zero.

502 A second explanation can be found in the integral formulation of the impermeability
 503 theorem derived in Haynes & McIntyre (1990) and discussed in Morel & McWilliams (2001):

$$\frac{d}{dt} \iiint_{\Omega} d\Omega \Delta Q = -f \frac{d\Omega}{dt}, \quad (21)$$

504 where Ω is a domain with periodic boundary conditions or with no normal flow (our case
 505 here), $d\Omega$ a volume element, ΔQ the PV anomaly with respect to the PV background, and
 506 $\frac{d\Omega}{dt}$ the volume variations of the layer. This formulation states that the bulk integral of the
 507 PV anomaly can only be changed by a loss or a gain of the volume inside a layer comprised
 508 between two isopycnals. At $t \sim 120$ days, the frontogenesis at the edge of the eddy has led to
 509 an isopycnal steepening at the surface. In particular, the layer between the $\rho = 1024.4 \text{ kg m}^{-3}$
 510 and the $\rho = 1024.5 \text{ kg m}^{-3}$ isopycnals is thin, and slopes very steeply towards the surface.
 511 This specific layer is chosen because it represents isopycnals outcropping at the edge of the
 512 eddy. Then, after the destabilization of the eddy edge and diapycnal mixing, this layer has
 513 become thicker, and the front is less steep, see Appendix D, Fig. D.20. Following eq. (21),
 514 this change of thickness leads to the decrease of the bulk integral of the PV, which explains
 515 the decrease of local PV, and the formation of negative PV. In Fig. 13, we present the time
 516 evolution of this layer volume. It is fairly consistent with the appearance of negative PV.

517 The presence of locally negative PV, along with an examination of the Richardson number
 518 show that the edge of the eddy is subject to SI. The area where $Ri < Ri_c$ is indicated in
 519 Fig. 14(top). In this area, the PV of the geostrophic flow is negative. When the PV changes
 520 sign, due to the second and third terms in eq. (2), SI develops. From $t \sim 160$ days, the edge
 521 of the eddy thus becomes strongly deformed by vorticity changes over scales of $O(1)$ km. SI

522 then propagates inward. At the end of the simulation, at $t = 300$ days, the SI pattern is
 523 present in the whole core of the eddy, at the surface, see Fig. 3(d).

524 4. Sensitivity study

525 We have performed other simulations to study the sensitivity of our results to the nu-
 526 merical setup. Hereafter, the 'reference simulation' refers to the simulation on the f -plane,
 527 with a cyclonic eddy, $\Delta x = 1$ km, 256 vertical levels, and the numerical settings discussed
 528 in section 2.2. All the sensitivity tests are performed by varying one or several of these
 529 parameters. The details of these simulations are not shown in this paper, but we mention
 530 their most salient features.

531 Firstly, we changed the numerical settings of the model. Changing the horizontal ad-
 532 vection scheme to a third-order upwind advection scheme (UP3) leads to a larger implicit
 533 viscosity, and the fronts at the surface are less intense and become unstable later than in the
 534 reference run. Fewer small vortices result from the instability and they are less intense. If
 535 we remove the KPP-scheme parameterization in the interior, an important noise appears at
 536 $t \sim 30$ days because of a lack of vertical turbulent closure. The sensitivity on the boundary
 537 conditions has been tested by running the model in a larger domain (1000×2000 km) with
 538 the eddy initialized at $(x_0, y_0) = (400, 300)$ km. This does not affect the dynamics of the
 539 eddy.

540 Secondly, we performed the reference simulation with a flat bottom at 4000 m with the
 541 same number and stretching of vertical levels. This does not affect the primary instabilities
 542 (the growth of mode 2 and the formation of row of small vortices), showing that a bottom
 543 at 1500 m is sufficient to describe the dynamic of the eddy. However, the SI occurs 30 days
 544 earlier. This is due to the fact that the spacing between the vertical levels is larger than in
 545 the reference run. The $\Delta x/\Delta z$ ratio is not close enough to N/f_0 , and the frontal dynamic
 546 is not well resolved.

547 Thirdly, we tested the cyclone-anticyclone asymmetry. We initialized the opposite com-
 548 posite density anomaly and recalculated the temperature and the velocity fields associated
 549 with it. This produces a warm core anticyclonic eddy. We put this structure in the same
 550 stratification as for the reference simulation, and we ran the model. We observed a different

551 evolution than for the cyclonic case. At $t = 100$ days, the anticyclone was still stable, and
 552 its horizontal shape was similar to its initial shape. An azimuthal mode 2 then grew, as
 553 in the cyclonic case. It led to the formation of a tripole with spiral arms at $t \sim 280$ days.
 554 Then, the arms also became unstable and formed submesoscale vortices of negative relative
 555 vorticity. For the anticyclone, the growth of the perturbation was much slower than for
 556 the cyclone. Furthermore, the two satellites in the formed tripole were smaller than in the
 557 reference simulation. This asymmetry can be explained as follows. Considering the cyclo-
 558 geostrophic balance, a cyclone and an anticyclone cannot have both antisymmetric velocity
 559 and density anomalies. Here, we initialized the anticyclone with the density anomaly. Thus,
 560 its swirling velocity was smaller than that of the cyclone, and the initial anticyclone had a
 561 weaker kinetic energy. In Stegner & Dritschel (2000), a comparison between the shape of
 562 tripoles obtained from the destabilization of a cyclone and an anticyclone can be seen in
 563 their Fig. 7.

564 Finally, we performed the reference simulation, but now on a β -plane, with $\beta = 2.1 \cdot 10^{-11} \text{ m}^{-1} \text{ s}^{-1}$
 565 (the mean value of β in the area of the composite eddy). The primary instability of the eddy
 566 strongly differs from the f -plane simulations. After 20 days of simulation, the eddy starts
 567 drifting northwestward, with a trailing Rossby wave wake. The evolution of the eddy is simi-
 568 lar to that shown in Fig. 3 of McWilliams et al. (1986). Then, mode 2 grows. At $t \sim 70$ days,
 569 two asymmetric arms are present around the initial eddy. They become unstable similarly
 570 as in the reference simulation, creating submesoscale vortices around the initial eddy.

571 5. Discussion

572 5.1. On the stability of the composite eddy

573 In this paper, we studied the stability of a composite cyclone as revealed by Argo floats
 574 in the northern Arabian Sea. With this simulation, we were able to study numerous kinds
 575 of instabilities, thanks to very high horizontal and vertical resolutions.

576 First, we observed that a deep azimuthal mode 2 barotropic instability deforms the eddy,
 577 which eventually evolves into a tripole after about 4 months of simulation. This kind of
 578 instability has already been observed for specific 2D analytical barotropic shielded vortices
 579 (Carton & McWilliams, 1989; Stegner & Dritschel, 2000), 3D meddy-like eddies (Yim &

580 Billant, 2015; Meunier et al., 2015; Ménesguen et al., 2018), or surface eddies (Meunier
581 et al., 2019). We show that in the vicinity of a realistic eddy intensified at the surface,
582 azimuthal mode 2 perturbations is the main driver for its deformation.

583 Second, we showed that a baroclinic instability together with the presence of a critical
584 level for the most unstable mode is the main cause for the generation of a highly ageostrophic
585 flow around the eddy. This generates sharp fronts in the surface mixed layer where the Rossby
586 number is large ($\epsilon > 1$).

587 Third, these fronts become unstable to a barotropic instability in the surface mixed
588 layer. This leads to the generation of submesoscale cyclones and filaments. This highlights
589 the predominance of secondary instabilities in the evolution of isolated eddies.

590 Finally, our results indicate that symmetric instability may be ubiquitous in large oceanic
591 vortices, even cyclonic ones. Indeed, for small Bu vortices, the critical level is located near
592 the edge of the eddy (Nguyen et al., 2012) where energy is concentrated. This leads to
593 the formation of intense fronts. Near these fronts, a strongly imbalanced circulation occurs,
594 and yields diapycnal mixing. As previously observed in the context of idealized simulations
595 (Nadiga, 2014; Brannigan et al., 2017), this causes PV to change sign locally, and SI develops
596 at the edge of the cyclonic eddy. This happens when the edge of the eddy becomes unstable
597 due to the interaction between submesoscale vortices and the large eddy. It highlights the
598 fact that in the real ocean the interactions between small scale features and large mesoscale
599 eddies may play a key role in the stability of the latter.

600 Previous studies considering analytical vortices showed that when a vortex is unstable, it
601 may break into smaller vortices, depending on its initial profile (Carton et al., 1989; Stegner
602 & Dritschel, 2000). A major result of this study is that even if instabilities occur, the
603 composite eddy is not destroyed and remains as a large scale coherent structure for the last
604 6 months of the simulation, similar to specific kind of analytical vortices (Hua et al., 2013;
605 Ménesguen et al., 2018). The composite re-stabilizes into a tripolar structure for which the
606 positive vorticity pole is slightly elliptical but coherent.

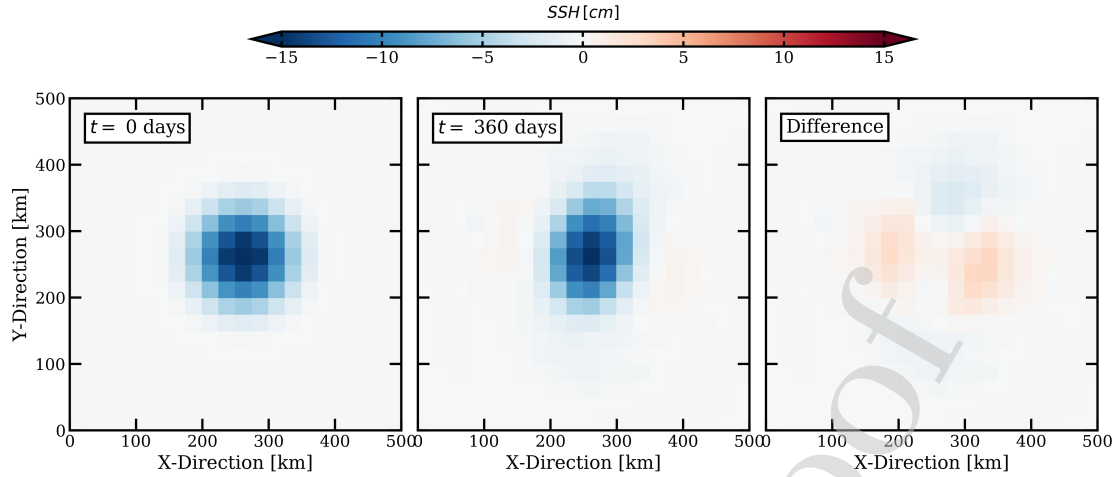


Figure 15: SSH signature of the eddy at initialization (left), at the end of the simulation ($t = 360$ days) (middle), and the difference between the two. The resolution of the plot is downgraded to the same resolution as the altimetric product used to generate the composite eddy.

607 5.2. On the detectability of eddy instabilities

608 To infer the detectability in altimeter products of the series of instabilities described in
 609 this paper, we computed the SSH signature of the eddy at the beginning and at the end of the
 610 simulation, using a downgraded resolution similar to the one of the altimetric product (Fig.
 611 15). The signature of the tripole at the end of the simulation is that of an elliptical cyclonic
 612 eddy, of ellipticity $e=0.72$. The difference between the tripole and the initial cyclone is very
 613 weak, with variations of SSH of $O(1)$ cm, which is of the order of magnitude of the formal
 614 error induced by the spatio-temporal interpolation of altimetric products (see Appendix A
 615 in de Marez et al. (2019)). This indicates that the tripolar structures often observed in
 616 numerical studies may be present in the ocean but may not be observed due to the coarse
 617 resolution of the altimetry.

618 The mean ellipticity of eddies used to compute the composite was on average 0.75. The
 619 cyclone at the end of the simulation thus have an ellipticity comparable with the ellipticity of
 620 eddies observed in altimetric products, which were used to compute the composite. Since the
 621 composite was computed assuming axisymmetry, it is of interest to assess the impact of this
 622 hypothesis on the final state of the modelled eddy, by computing an azimuthal average (Fig.
 623 16). The differences between the initialization and the final form act over scale of $O(10)$ km
 624 on the horizontal and $O(10)$ m on the vertical. Considering the very coarse resolution of the

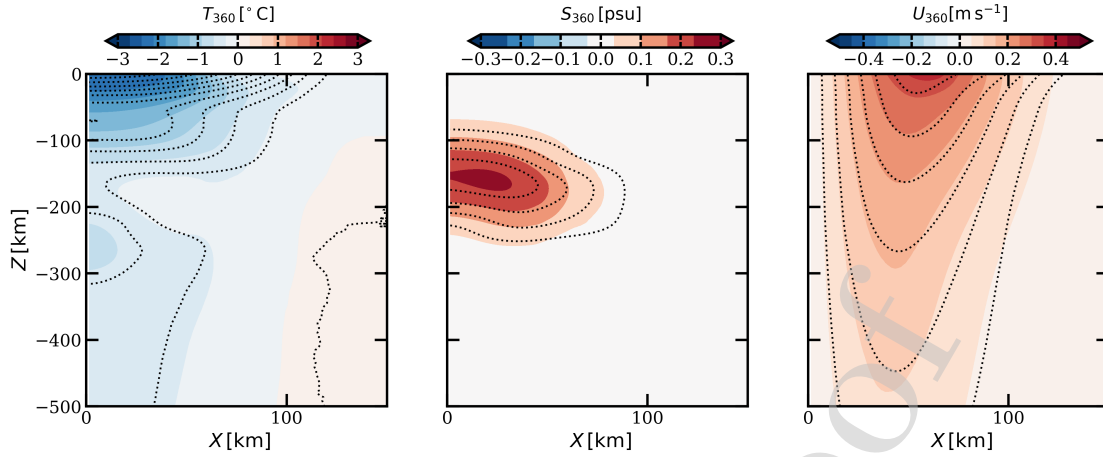


Figure 16: Comparison between the azimuthal average of the final form of the eddy (at $t = 360$ days) and the composite. Color contours are azimuthal averages of the final eddy while black dashed contours indicate the same contours for the initial eddy.

625 dataset available to study the 3D structure of eddies (*e.g.* $O(10)$ km for the altimetric product
 626 and $O(10)$ m for Argo floats), and the error implied by the composite method $O(1 - 5)$ km
 627 (Chaigneau et al., 2011), these differences can not be seen with *in situ* data.

628 The small scale features we observe during the secondary instabilities can be observed
 629 qualitatively on snapshots of true color (Lévy et al., 2018) or of sea surface temperature
 630 (Buckingham et al., 2017). However, no altimetric product allowing to predict the dynamical
 631 quantities at this resolution are currently available. This means that neither the primary
 632 instability nor the secondary instabilities can be clearly captured in a systematic way using
 633 the currently available altimetric and floats data. Considering SSH only, the composite eddy
 634 we studied evolves little, and fairly represents the eddy observed in the altimetry which can
 635 live for several months.

636 Appendix A. Maps of energy transfer terms

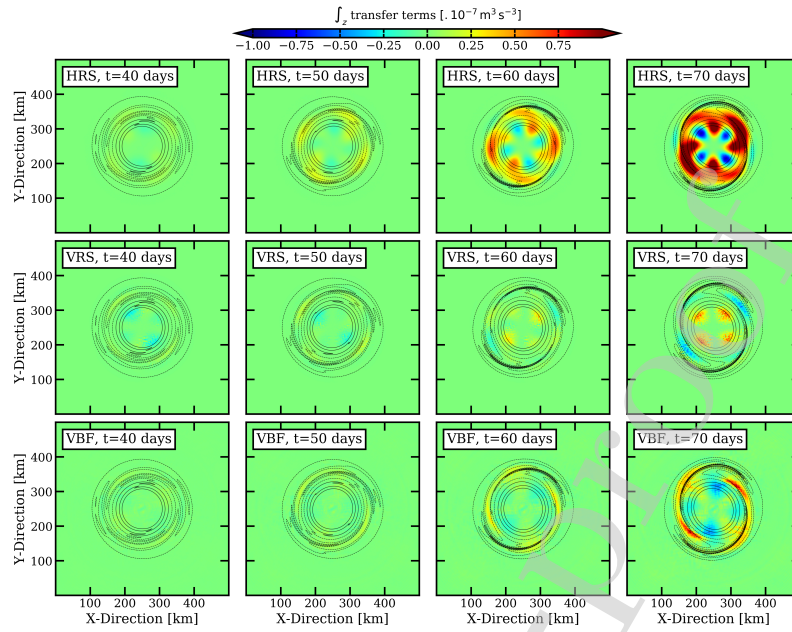


Figure A.17: Snapshots of energy transfer terms integrated on the vertical at $t = 40, 50, 60,$ and 70 days (from left to right). HRS, VRS, and VBF stand for Horizontal Reynolds Stress, Vertical Reynolds Stress, and Vertical Buoyancy Flux.

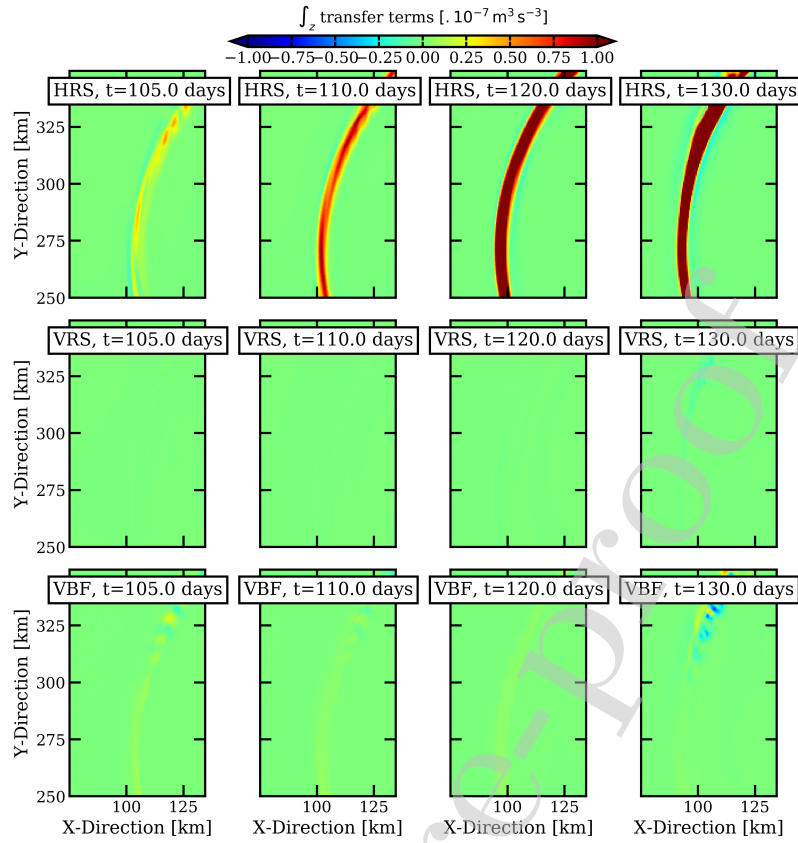


Figure A.18: Snapshots of energy transfer terms integrated on the vertical, zoom on the left spiral arm which becomes unstable, at $t = 105, 110, 120,$ and 130 days (from left to right).

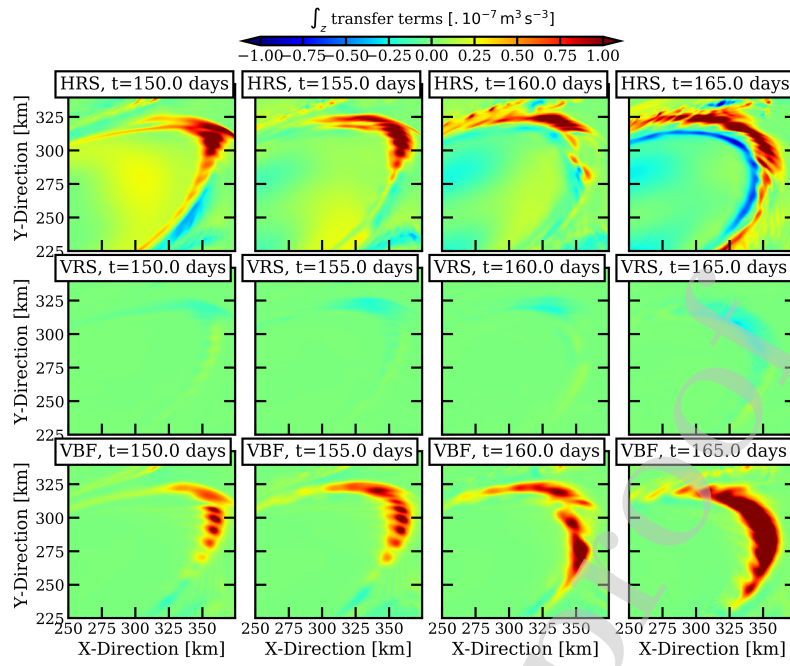


Figure A.19: Snapshots of energy transfer terms integrated on the vertical, zoom on the edge of the eddy which becomes unstable, at $t = 150, 155, 160,$ and 165 days (from left to right).

637 **Appendix B. Estimating the phase velocity of the perturbation in the QG ap-**
 638 **proximation**

639 To estimate the value of the phase velocity of the mode 2 perturbation, one can use
 640 the framework of the continuously stratified quasi-geostrophic (QG) model (Vallis, 2017).
 641 We consider a mean state which is a circular barotropic eddy of azimuthal velocity U_θ
 642 and potential vorticity \bar{q} . We introduce a perturbation in the form of a normal mode, of
 643 potential vorticity q' and current function ψ' . Linearizing the system around the mean state
 644 gives (Pedlosky, 2013):

$$(U_\theta - c)q' - \psi' \bar{q}_r = 0 \quad (\text{B.1})$$

645 where c is the azimuthal velocity of the perturbation and \bar{q}_r is the radial derivative of \bar{q} . The
 646 potential vorticity of the perturbation is

$$q' = \Delta\psi' + \frac{f_0^2}{N_0^2} \partial_z \psi' = L\psi'. \quad (\text{B.2})$$

647 N_0 is the ambient stratification of the flow, which is in our case $\sim 10^{-2} \text{ s}^{-1}$. Using (B.1) and
 648 (B.2), the azimuthal velocity of the perturbation can be expressed as:

$$c = U_\theta - \frac{\psi' \bar{q}_r}{L\psi'}. \quad (\text{B.3})$$

649 For our purpose, we only discuss the order of magnitude of the velocity of the perturbation,
 650 which is:

$$c \sim U_\theta - \frac{\bar{q}_r}{\alpha}, \quad (\text{B.4})$$

651 where α approximates the operator L such as:

$$\alpha = \underbrace{\frac{4\pi^2}{R^2} + \left(\frac{m}{R}\right)^2}_{\alpha_{BT}} + \underbrace{\frac{f_0^2}{h N_0^2}}_{\alpha_{BC}}, \quad (\text{B.5})$$

652 with m the azimuthal mode of the perturbation, $R \sim 100$ km the radius of the eddy and
 653 $h \sim 50$ m the typical scale of variation of the perturbation. The first two terms (α_{BT})

654 represent the barotropic perturbation, while the third one (α_{BC}) corresponds to the vortex
 655 stretching induced by the baroclinicity of the flow.

656 In the case we study here, $\bar{q}_r \sim \frac{U_\theta^{max}}{(R/2)^2}$, with $U_\theta^{max} \sim 0.5 \text{ m s}^{-1}$ the value of U_θ at $\sim R/2$.
 657 This gives $\bar{q}_r \sim 2 \cdot 10^{-10} \text{ m}^{-1} \text{ s}^{-1}$, $\alpha_{BT} \sim 1.4 \cdot 10^{-9} \text{ m}^{-2}$ and $\alpha_{BC} \sim 5 \cdot 10^{-9} \text{ m}^{-2}$. At the edge
 658 of the eddy, $U_\theta \sim 0.1 \text{ m s}^{-1}$. Using eq. (B.4) gives an estimation of the phase velocity
 659 $c \sim 0.06 \text{ m s}^{-1}$. This corresponds to a velocity of $0.06 \text{ rad days}^{-1}$, which is in fairly good
 660 agreement with the phase velocity computed in the simulation, and seen in Fig. 8. Notice
 661 that this estimation of the phase velocity depends on the values chosen for each quantity,
 662 and does not take into account the baroclinicity of the mean flow. However, it shows that
 663 to obtain a proper estimation, we need to consider both the BT and the BC components of
 664 the perturbation.

665 **Appendix C. How can diapycnal mixing change the sign of the PV ?**

666 As pointed in Morel & McWilliams (2001), *'when mixing does occur, it is not easy to*
 667 *predict the change of the PV for a fluid parcel'*. Using the Ertel form of the PV, we assess
 668 here how can diapycnal mixing change the sign of the PV.

669 In the case of a front localized at the edge of an axisymmetric eddy, with no radial
 670 velocity, one can write the PV in polar coordinates as:

$$Q = \zeta_a \partial_z b + (\partial_z u_\theta)(\partial_r b),$$

671 with $\zeta_a = \zeta + f_0$. If we consider the Thermal Wind Balance, this becomes

$$Q = \zeta_a \partial_z b - f^{-1}(\partial_r b)^2.$$

672 We study the variations of PV when the buoyancy is modified by diapycnal mixing. We
 673 introduce $\Delta_z b$ and $\Delta_r b$ the variations of buoyancy respectively along the z and r axis. The
 674 value of Q may thus be approximated by:

$$Q = \frac{\Delta_z b}{\Delta z} \zeta_a - f^{-1} \left(\frac{\Delta_r b}{\Delta r} \right)^2. \quad (\text{C.1})$$

675 If diapycnal mixing occurs, the gradients of buoyancy diminish along the z -axis and/or the
 676 r -axis. In terms of variations of buoyancy, we thus have

$$\begin{cases} \Delta_z b \rightarrow \Delta_z b - b_{z*} \\ \Delta_r b \rightarrow \Delta_r b - b_{r*}, \end{cases} \quad (\text{C.2})$$

677 where $b_{r*} > 0$ and $b_{z*} > 0$ are the variations of buoyancy induced by the diapycnal mixing.
 678 They are positive since diapycnal mixing leads to a decrease of the variations of buoyancy.
 679 We assume here that during the time in which diapycnal mixing occurs, the flow does not
 680 vary, and ζ_a thus remains constant. This strong assumption is not true at long times, when
 681 the new circulation is adjusted, but it allows to keep the calculation and the reasoning simple.

682 We define Q^* as the PV value after the diapycnal mixing. Introducing the new buoyancy
 683 variations (C.2) in the expression of the PV (C.1) gives:

$$Q^* = \underbrace{\frac{\Delta_z b}{\Delta z} \zeta_a - f^{-1} \left(\frac{\Delta_r b}{\Delta r} \right)^2 - \frac{b_{z^*}}{\Delta z} \zeta_a - f^{-1} \left(\frac{b_{r^*}}{\Delta r} \right)^2}_Q + 2f^{-1} \frac{\Delta_r b b_{r^*}}{(\Delta r)^2}.$$

684 The two first terms on the right hand side are the PV before the diapycnal mixing. We then
 685 define $\Delta Q = Q^* - Q$, the variation of PV during the diapycnal mixing. It is expressed such
 686 as:

$$\Delta Q = \underbrace{-\frac{b_{z^*}}{\Delta z} \zeta_a}_{\Delta Q_1} - \overbrace{f^{-1} \left(\frac{b_{r^*}}{\Delta r} \right)^2}^{\Delta Q_2} + \underbrace{2f^{-1} \frac{\Delta_r b b_{r^*}}{(\Delta r)^2}}_{\Delta Q_3}.$$

687 If the vorticity in the flow is positive, and if it is located in the northern hemisphere,
 688 $\zeta_a > 0$. Thus, both ΔQ_1 and ΔQ_2 are strictly negative. The sign of ΔQ_3 depends on the sign
 689 of $\Delta_r b$. In the case of a front leading to a positive velocity along the θ -axis (*e.g* at the edge
 690 of a cyclone), the buoyancy gradients along the r -direction are positive. Then, $\Delta Q_3 > 0$ and
 691 the sign of ΔQ thus depends on the relative importance of its terms. The sign of ΔQ thus
 692 depends on the scale of variations and the values of the gradients. For instance, in a case
 693 where the mixing only occurs on the vertical, $b_{r^*} = 0$. The variation of PV thus reduces to
 694 $\Delta Q = \Delta Q_1 < 0$. In this case, the PV decreases. If before the mixing it was already close to
 695 0, the decrease of the PV can thus lead to the generation of negative PV where the fluid has
 696 been mixed. A summary of the possible sign that ΔQ can take depending on the direction
 697 of the current, and the direction of the mixing is shown in Table C.1.

	ΔQ_1	ΔQ_2	ΔQ_3	ΔQ
CE	< 0	< 0	> 0	?
AE	> 0	< 0	< 0	?
CE vert.	< 0	$= 0$	$= 0$	< 0
AE vert.	> 0	$= 0$	$= 0$	> 0
CE horiz.	$= 0$	< 0	> 0	?
AE horiz.	$= 0$	< 0	< 0	< 0

Table C.1: Summary of the sign that can take ΔQ . CE and AE designate cyclonic and anticyclonic flow; vert. and horiz. indicate cases where the mixing only occurs on the vertical direction or the horizontal direction; ? indicates that the sign of ΔQ depends on the relative importance of the different terms.

698 Appendix D. Section of the front at the edge of the eddy

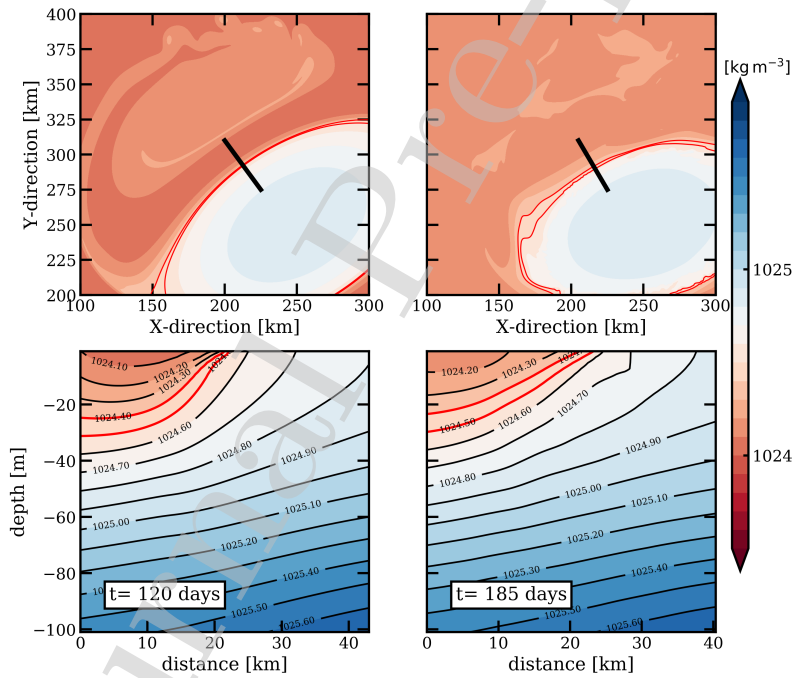


Figure D.20: (top) Snapshots of density at the surface at $t = 120$ days (left) and $t = 185$ days (right). (bottom) Vertical sections of density at $t = 120$ days (left) and $t = 185$ days (right), their position is shown by the black thick lines in the top panels. Red contours indicates the isopycnals surrounding the layer we discuss, for which we compute the volume shown in Fig. 13

699 **Acknowledgments**

700 This work was funded by the Direction Générale de l'Armement (DGA) *via* a full grant
701 for Charly de Marez's PhD. This work is also a contribution to PRC 1069 'Meso and subme-
702 soscale vortices in the Atlantic and Indian Ocean', funded by CNRS and RFBR. Simulations
703 were performed using the HPC facilities DATARMOR of 'Pôle de Calcul Intensif pour la
704 Mer' at Ifremer, Brest, France. The authors thank N. Lahaye for helpful discussions, and
705 the two anonymous reviewers whose remarks improved the contents of this paper. Model
706 output is available upon request.

707 **References**

- 708 Al Saafani, M. A., Shenoi, S. S. C., Shankar, D., Aparna, M., Kurian, J., Durand, F., &
709 Vinayachandran, P. N. (2007). Westward movement of eddies into the Gulf of Aden from
710 the Arabian Sea. *Journal of Geophysical Research*, *112*, C11. doi:10.1029/2006JC004020.
- 711 Armi, L., Hebert, D., Oakey, N., Price, J. F., Richardson, P. L., Rossby, H. T., & Ruddick,
712 B. (1989). Two Years in the Life of a Mediterranean Salt Lens. *Journal of Physical*
713 *Oceanography*, *19*, 354–370. doi:10.1175/1520-0485(1989)019<0354:TYITLO>2.0.CO;2.
- 714 Bell, M. J. (2018). Reduction of the linear stability problem for general zonal flows with any
715 Rossby and Richardson numbers to a PDE. *Quarterly Journal of the Royal Meteorological*
716 *Society*, *144*, 2260–2276. doi:10.1002/qj.3352.
- 717 Brannigan, L., Marshall, D. P., Naveira Garabato, A. C., Nurser, A. J. G., & Kaiser, J.
718 (2017). Submesoscale Instabilities in Mesoscale Eddies. *Journal of Physical Oceanography*,
719 *47*, 3061–3085. doi:10.1175/JPO-D-16-0178.1.
- 720 Bretherton, F. P. (1966). Critical layer instability in baroclinic flows. *Quarterly Journal of*
721 *the Royal Meteorological Society*, *92*, 325–334. doi:10.1002/qj.49709239302.
- 722 Buckingham, C. E., Khaleel, Z., Lazar, A., Martin, A. P., Allen, J. T., Naveira Garabato,
723 A. C., Thompson, A. F., & Vic, C. (2017). Testing Munk’s hypothesis for submesoscale
724 eddy generation using observations in the North Atlantic. *Journal of Geophysical Research:*
725 *Oceans*, *122*, 6725–6745. doi:10.1002/2017JC012910.
- 726 Carton, X., & McWilliams, J. (1989). Barotropic and Baroclinic Instabilities of Axisymmet-
727 ric Vortices in a Quasigeostrophic Model, . *50*, 225–244. doi:10.1016/S0422-9894(08)
728 70188-0.
- 729 Carton, X. J., Flierl, G. R., & Polvani, L. M. (1989). The Generation of Tripoles from
730 Unstable Axisymmetric Isolated Vortex Structures. *Europhysics Letters (EPL)*, *9*, 339–
731 344.

- 732 Chaigneau, A., Le Texier, M., Eldin, G., Grados, C., & Pizarro, O. (2011). Vertical
733 structure of mesoscale eddies in the eastern South Pacific Ocean: A composite analy-
734 sis from altimetry and Argo profiling floats. *Journal of Geophysical Research*, *116*, C11.
735 doi:10.1029/2011JC007134.
- 736 Chelton, D. B., deSzoeke, R. A., Schlax, M. G., El Naggar, K., & Siwertz, N. (1998).
737 Geographical Variability of the First Baroclinic Rossby Radius of Deformation. *Journal of*
738 *Physical Oceanography*, *28*, 433–460. doi:10.1175/1520-0485(1998)028<0433:GVOTFB>
739 2.0.CO;2.
- 740 Chelton, D. B., Gaube, P., Schlax, M. G., Early, J. J., & Samelson, R. M. (2011). The
741 Influence of Nonlinear Mesoscale Eddies on Near-Surface Oceanic Chlorophyll. *Science*,
742 *334*, 6054. doi:10.1126/science.1208897.
- 743 de Marez, C., L'Hégaret, P., Morvan, M., & Carton, X. (2019). On the 3d structure of
744 eddies in the Arabian Sea. *Deep Sea Research Part I: Oceanographic Research Papers*,
745 *150*, 103057. doi:10.1016/j.dsr.2019.06.003.
- 746 Dong, C., McWilliams, J. C., Liu, Y., & Chen, D. (2014). Global heat and salt transports
747 by eddy movement. *Nature Communications*, *5*, 3294. doi:10.1038/ncomms4294.
- 748 Eliassen, A. (1983). The Charney—Stern Theorem on Barotropic—Baroclinic Instability, .
749 (pp. 563–572). doi:10.1007/978-3-0348-6608-8_11.
- 750 Fjørtoft, R. (1950). Application of integral theorems in deriving criteria of stability for
751 laminar flows and for the baroclinic circular vortex, .
- 752 Flierl, G. R. (1988). On the instability of geostrophic vortices. *Journal of fluid mechanics*,
753 *197*, 349–388. doi:10.1017/S0022112088003283.
- 754 Gent, P. R., & McWilliams, J. C. (1986). The instability of barotropic circular vortices. *Geo-*
755 *physical & Astrophysical Fluid Dynamics*, *35*, 209–233. doi:10.1080/03091928608245893.
- 756 Gula, J., Molemaker, M. J., & McWilliams, J. C. (2015). Gulf Stream Dynamics along
757 the Southeastern U.S. Seaboard. *Journal of Physical Oceanography*, *45*, 690–715. doi:10.
758 1175/JPO-D-14-0154.1.

- 759 Gula, J., Molemaker, M. J., & McWilliams, J. C. (2016). Topographic generation of subme-
760 soscale centrifugal instability and energy dissipation. *Nature Communications*, *7*, 12811.
761 doi:10.1038/ncomms12811.
- 762 Halo, I., Backeberg, B., Penven, P., Ansorge, I., Reason, C., & Ullgren, J. (2014). Eddy prop-
763 erties in the Mozambique Channel: A comparison between observations and two numerical
764 ocean circulation models. *Deep Sea Research Part II: Topical Studies in Oceanography*,
765 *100*, 38–53. doi:10.1016/j.dsr2.2013.10.015.
- 766 Haynes, P. H., & McIntyre, M. E. (1990). On the Conservation and Impermeability Theorems
767 for Potential Vorticity. *Journal of the Atmospheric Sciences*, *47*, 2021–2031. doi:10.1175/
768 1520-0469(1990)047<2021:OTCAIT>2.0.CO;2.
- 769 Hoskins, B. (1982). The mathematical theory of frontogenesis. *Annual review of fluid me-*
770 *chanics*, *14*, 131–151. doi:10.1146/annurev.fl.14.010182.001023.
- 771 Hoskins, B. J. (1974). The role of potential vorticity in symmetric stability and instability.
772 *Quarterly Journal of the Royal Meteorological Society*, *100*, 480–482. URL: <http://doi.wiley.com/10.1002/qj.49710042520>. doi:10.1002/qj.49710042520.
- 774 Hoskins, B. J., McIntyre, M. E., & Robertson, A. W. (1985). On the use and significance of
775 isentropic potential vorticity maps. *Quarterly Journal of the Royal Meteorological Society*,
776 *111*, 877–946. doi:10.1002/qj.49711147002.
- 777 Hua, B. L., Ménesguen, C., Le Gentil, S., Schopp, R., Marsset, B., & Aiki, H. (2013).
778 Layering and turbulence surrounding an anticyclonic oceanic vortex: in situ observations
779 and quasi-geostrophic numerical simulations. *Journal of Fluid Mechanics*, *731*, 418–442.
780 doi:10.1017/jfm.2013.369.
- 781 Isern-Fontanet, J., Lapeyre, G., Klein, P., Chapron, B., & Hecht, M. W. (2008). Three-
782 dimensional reconstruction of oceanic mesoscale currents from surface information. *Journal*
783 *of Geophysical Research: Oceans*, *113*, C9. doi:10.1029/2007JC004692.
- 784 Keppler, L., Cravatte, S., Chaigneau, A., Pegliasco, C., Gourdeau, L., & Singh, A. (2018).
785 Observed Characteristics and Vertical Structure of Mesoscale Eddies in the Southwest

- 786 Tropical Pacific. *Journal of Geophysical Research: Oceans*, *123*, 2731–2756. doi:10.1002/
787 2017JC013712.
- 788 Klein, P., Hua, B. L., Lapeyre, G., Capet, X., Le Gentil, S., & Sasaki, H. (2008). Upper Ocean
789 Turbulence from High-Resolution 3D Simulations. *Journal of Physical Oceanography*, *38*,
790 1748–1763. doi:10.1175/2007JP03773.1.
- 791 Large, W. G., McWilliams, J. C., & Doney, S. C. (1994). Oceanic vertical mixing: A review
792 and a model with a nonlocal boundary layer parameterization. *Reviews of Geophysics*,
793 *32*, 363–403. doi:10.1029/94RG01872.
- 794 Le Vu, B., Stegner, A., & Arsouze, T. (2018). Angular Momentum Eddy Detection and
795 Tracking Algorithm (AMEDA) and Its Application to Coastal Eddy Formation. *Journal*
796 *of Atmospheric and Oceanic Technology*, *35*, 739–762. doi:10.1175/JTECH-D-17-0010.1.
- 797 Lévy, M., Franks, P. J. S., & Smith, K. S. (2018). The role of submesoscale cur-
798 rents in structuring marine ecosystems. *Nature Communications*, *9*, 4758. doi:10.1038/
799 s41467-018-07059-3.
- 800 L'Hégaret, P., Beal, L. M., Elipot, S., & Laurindo, L. (2018). Shallow Cross-Equatorial
801 Gyres of the Indian Ocean Driven by Seasonally Reversing Monsoon Winds. *Journal of*
802 *Geophysical Research: Oceans*, (pp. 8902–8920). doi:10.1029/2018JC014553.
- 803 L'Hégaret, P., Carton, X., Louazel, S., & Boutin, G. (2016). Mesoscale eddies and sub-
804 mesoscale structures of Persian Gulf Water off the Omani coast in spring 2011. *Ocean*
805 *Science*, *12*, 687–701. doi:10.5194/os-12-687-2016.
- 806 L'Hégaret, P., Duarte, R., Carton, X., Vic, C., Ciani, D., Baraille, R., & Corréard, S.
807 (2015). Mesoscale variability in the Arabian Sea from HYCOM model results and ob-
808 servations: impact on the Persian Gulf Water path. *Ocean Science*, *11*, 667–693.
809 doi:10.5194/os-11-667-2015.
- 810 Li, L., Nowlin, W. D., & Jilan, S. (1998). Anticyclonic rings from the Kuroshio in the South
811 China Sea. *Deep Sea Research Part I: Oceanographic Research Papers*, *45*, 1469–1482.
812 doi:10.1016/S0967-0637(98)00026-0.

- 813 McDougall, T. J., & Barker, P. M. (2011). *Getting started with TEOS-10 and the Gibbs*
814 *Seawater (GSW), Oceanographic Toolbox.*
- 815 McWilliams, J. C. (1985). Submesoscale, coherent vortices in the ocean. *Reviews of Geo-*
816 *physics, 23*, 165–182. doi:10.1029/RG023i002p00165.
- 817 McWilliams, J. C., Gent, P. R., & Norton, N. J. (1986). The Evolution of Balanced, Low-
818 Mode Vortices on the β -Plane. *Journal of Physical Oceanography, 16*, 838–855. doi:https:
819 //doi.org/10.1175/1520-0485(1986)016<0838:TEOBLM>2.0.CO;2.
- 820 Ménesguen, C., Le Gentil, S., Marchesiello, P., & Ducouso, N. (2018). Destabilization of
821 an Oceanic Meddy-Like Vortex: Energy Transfers and Significance of Numerical Settings.
822 *Journal of Physical Oceanography, 48*, 1151–1168. doi:10.1175/jpo-d-17-0126.1.
- 823 Meunier, T., Ménesguen, C., Carton, X., Le Gentil, S., & Schopp, R. (2018). Optimal
824 perturbations of an oceanic vortex lens. *Fluids, 3*, 63. doi:10.3390/fluids3030063.
- 825 Meunier, T., Ménesguen, C., Schopp, R., & Le Gentil, S. (2015). Tracer Stirring around
826 a Meddy: The Formation of Layering. *Journal of Physical Oceanography, 45*, 407–423.
827 doi:10.1175/JPO-D-14-0061.1.
- 828 Meunier, T., Pallas-Sanz, E., Ruiz-Angulo, A., Ochoa-de-la-Torre, J., & Tenreiro, M. (2019).
829 Observations of Layering under an Anticyclonic Warm-Core Ring in the Gulf of Mexico.
830 *Journal of Physical Oceanography, .* doi:10.1175/JPO-D-18-0138.1.
- 831 Meunier, T., Pallas-Sanz, E., Tenreiro, M., Portela, E., Ochoa, J., Ruiz-Angulo, A., &
832 Cusí, S. (2018). The Vertical Structure of a Loop Current Eddy. *Journal of Geophysical*
833 *Research: Oceans, 123*, 6070–6090. doi:10.1029/2018JC013801.
- 834 Morel, Y., & McWilliams, J. (2001). Effects of Isopycnal and Diapycnal Mixing on the
835 Stability of Oceanic Currents. *Journal of Physical Oceanography, 31*, 2280–2296. doi:10.
836 1175/1520-0485(2001)031<2280:E0IADM>2.0.CO;2.
- 837 Morel, Y. G., Darr, D. S., & Talandier, C. (2006). Possible Sources Driving the Poten-
838 tial Vorticity Structure and Long-Wave Instability of Coastal Upwelling and Downwelling
839 Currents. *Journal of Physical Oceanography, 36*, 875–896. doi:10.1175/JPO2899.1.

- 840 Nadiga, B. T. (2014). Nonlinear evolution of a baroclinic wave and imbalanced dissipation.
841 *Journal of Fluid Mechanics*, *756*, 965–1006. doi:10.1017/jfm.2014.464.
- 842 Nguyen, H. Y., Hua, B. L., Schopp, R., & Carton, X. (2012). Slow quasigeostrophic unstable
843 modes of a lens vortex in a continuously stratified flow. *Geophysical & Astrophysical Fluid*
844 *Dynamics*, *106*, 305–319. doi:10.1080/03091929.2011.620568.
- 845 Olson, D. B., & Evans, R. H. (1986). Rings of the Agulhas current. *Deep Sea Research Part*
846 *A. Oceanographic Research Papers*, *33*, 27–42. doi:10.1016/0198-0149(86)90106-8.
- 847 Pedlosky, J. (1964). The Stability of Currents in the Atmosphere and the Ocean: Part
848 I. *Journal of the Atmospheric Sciences*, *21*, 201–219. doi:10.1175/1520-0469(1964)
849 021<0201:TSOCIT>2.0.CO;2.
- 850 Pedlosky, J. (2013). *Geophysical Fluid Dynamics*. Springer Science & Business Media.
- 851 Penven, P., Halo, I., Pous, S., & Marié, L. (2014). Cyclogeostrophic balance in the
852 Mozambique Channel. *Journal of Geophysical Research: Oceans*, *119*, 1054–1067.
853 doi:10.1002/2013JC009528.
- 854 Richardson, P. L. (1983). Gulf Stream Rings. In A. R. Robinson (Ed.), *Eddies in Ma-*
855 *rine Science* (pp. 19–45). Berlin, Heidelberg: Springer Berlin Heidelberg. doi:10.1007/
856 978-3-642-69003-7_2.
- 857 Riedinger, X., & Gilbert, A. D. (2014). Critical layer and radiative instabilities in shallow-
858 water shear flows. *Journal of Fluid Mechanics*, *751*, 539–569. doi:10.1017/jfm.2014.303.
- 859 Ripa, P. (1991). General stability conditions for a multi-layer model. *Journal of Fluid*
860 *Mechanics*, *222*, 119–137. doi:10.1017/S0022112091001027.
- 861 Roulet, G., Capet, X., & Maze, G. (2014). Global interior eddy available potential energy
862 diagnosed from Argo floats. *Geophysical Research Letters*, *41*, 1651–1656. doi:10.1002/
863 2013GL059004.
- 864 Scharffenberg, M. G., & Stammer, D. (2010). Seasonal variations of the large-scale
865 geostrophic flow field and eddy kinetic energy inferred from the TOPEX/Poseidon and

- 866 Jason-1 tandem mission data. *Journal of Geophysical Research*, *115*, C2. doi:10.1029/
867 2008JC005242.
- 868 Schott, F. A., & McCreary, J. P. (2001). The monsoon circulation of the Indian Ocean.
869 *Progress in Oceanography*, *51*, 1–123. doi:10.1016/S0079-6611(01)00083-0.
- 870 Shchepetkin, A. F., & McWilliams, J. C. (2005). The regional oceanic modeling system
871 (ROMS): a split-explicit, free-surface, topography-following-coordinate oceanic model.
872 *Ocean Modelling*, *9*, 347–404. doi:10.1016/j.ocemod.2004.08.002.
- 873 Shchepetkin, A. F., & McWilliams, J. C. (2011). Accurate Boussinesq oceanic modeling with
874 a practical, “Stiffened” Equation of State. *Ocean Modelling*, *38*, 41–70. doi:10.1016/j.
875 ocemod.2011.01.010.
- 876 Snyder, C., Skamarock, W. C., & Rotunno, R. (1993). Frontal dynamics near and follow-
877 ing frontal collapse. *Journal of the atmospheric sciences*, *50*, 3194–3212. doi:10.1175/
878 1520-0469(1993)050<3194:FDNAFF>2.0.CO;2.
- 879 Stegner, A., & Dritschel, D. G. (2000). A Numerical Investigation of the Stability of Isolated
880 Shallow Water Vortices. *Journal of Physical Oceanography*, *30*, 2562–2573. doi:10.1175/
881 1520-0485(2000)030<2562:ANIOTS>2.0.CO;2.
- 882 Thomas, L. N., Taylor, J. R., Ferrari, R., & Joyce, T. M. (2013). Symmetric instability in
883 the Gulf Stream. *Deep Sea Research Part II: Topical Studies in Oceanography*, *91*, 96–110.
884 doi:10.1016/j.dsr2.2013.02.025.
- 885 Vallis, G. K. (2017). *Atmospheric and oceanic fluid dynamics*. Cambridge University Press.
- 886 Vic, C., Roulet, G., Carton, X., & Capet, X. (2014). Mesoscale dynamics in the Arabian
887 Sea and a focus on the Great Whirl life cycle: A numerical investigation using ROMS.
888 *Journal of Geophysical Research: Oceans*, *119*, 6422–6443. doi:10.1002/2014JC009857.
- 889 Yim, E., & Billant, P. (2015). On the mechanism of the Gent–McWilliams instability of
890 a columnar vortex in stratified rotating fluids. *Journal of Fluid Mechanics*, *780*, 5–44.
891 doi:10.1017/jfm.2015.426.

- 892 Young, W. R., & Chen, L. (1995). Baroclinic Instability and Thermohaline Gradient
893 Alignment in the Mixed Layer. *Journal of Physical Oceanography*, 25, 3172–3185.
894 doi:10.1175/1520-0485(1995)025<3172:BIATGA>2.0.CO;2.
- 895 Zhang, Z., Wang, W., & Qiu, B. (2014). Oceanic mass transport by mesoscale eddies.
896 *Science*, 345, 322–324. doi:10.1126/science.1252418.

Journal Pre-proof

Charly de Marez: Conceptualization, Methodology, Software, Writing- Original draft.

Thomas Meunier: Conceptualization, Methodology, Writing- Reviewing and Editing.

Mathieu Morvan: Software, Writing- Reviewing and Editing.

Pierre L'Hégaret: Writing- Reviewing and Editing.

Xavier Carton: Writing- Reviewing and Editing, Supervision, Funding acquisition.

Journal Pre-proof

All co-authors have seen and agree with the contents of the manuscript and there is no financial interest to report. We certify that the submission is original work and is not under review at any other publication.

Charly de Marez and co-authors

Journal Pre-proof